Journal of CO2 Utilization 95 (2025) 103079

Contents lists available at ScienceDirect

Journal of CO2 Utilization

journal homepage: www.elsevier.com/locate/jcou

CO_2 capture performance of K_2CO_3-activated biochars derived from the textile dyeing sludge and corncob

Yu Pan [a], Jiahui Lei [a], Zehuang Zhang [a], Fangfang Lou [a], Kun Song [a], Lanfang Huang [a], Jun Wang [b], Qunxing Huang [a,c,*]

[a] Institute for Thermal Power Engineering, Zhejiang University, Hangzhou 310027, China
[b] National Institute of Guangdong Advanced Energy Storage Co., Ltd., Guangzhou 510080, China
[c] Key Laboratory of Clean Energy and Carbon Neutrality of Zhejiang Province, Zhejiang University, Hangzhou 310027, China

ARTICLE INFO

Keywords:
Textile dyeing sludge
Ultra-micropores
CO_2 adsorption
Synergetic effect
Co-pyrolysis

ABSTRACT

The advancement of low-cost biochar derived from organic solid wastes is highly desirable, as it serves as an efficient and environmentally friendly absorbent for CO_2 abatement. Textile dyeing sludge (TDS) and corncob are two common types of carbonaceous solid wastes that are abundant and easily accessible. In this study, TDS and corncob were co-pyrolyzed to produce a series of CO_2 adsorption biochars (SCs). Results show that the synergetic and self-catalytic effects of the reaction between alkali/alkaline earth metals and the organic matters in TDS and corncob can increase biochar yield and enhance the ultra-micropore structure accounting for effective CO_2 adsorption. Moreover, the specific surface area of SC activated at 700 °C (SC700) was higher than corncob-based biochar. SC700 exhibited the highest CO_2 adsorption capacity (128.1 mg/g) among the SCs, which was more than double that of TDS biochar. This is primarily because SC700 had the highest specific surface area of ultra-micropores (544.38 m^2/g) and ultra-micropore volume (0.16 cm^3/g) among the SCs. After ten cycles tests, SC700 still showed good CO_2 adsorption-desorption performance, with a decrease of less than 1.5 %. The analysis of in situ DFIRT spectroscopy revealed that the CO_2 adsorption of SC700 involved both physical and chemical adsorption processes, with physical adsorption being dominant. This study provides an environmentally friendly and cost-effective method for the utilization of TDS and corncob to produce valuable biochar for CO_2 adsorption.

1. Introduction

The rapid development of global economy and population growth have led to significant energy consumption and carbon emissions, creating serious challenges for the global environment[1]. To address these issues, it is extremely urgent to promote green development through energy conservation and carbon emission reduction[2,3]. Adsorption is a promising strategy for CO_2 capture. Various CO_2 adsorbents have been developed, including zeolites, silicas, porous organic polymers, covalent organic frameworks, and metal-organic structures [4]. However, their application still faces limitations such as high costs, difficulties in regeneration and competition during adsorption[5]. In contrast, biochar is recognized as a negative carbon material and has gained significant attention due to its advantages[6]. These advantages include a large specific surface area, high CO_2 adsorption capacity, low energy consumption for regeneration, and relatively low cost[5]. As a result, biochar is considered a promising CO_2 adsorbent material[7].

Organic solid wastes generated from daily human activities and industrial manufacturing processes such as sludge, coal slime, waste tires, waste plastics, and biomass, are abundant, cost-effective, and possess a relatively high carbon content[8]. These characteristics make them valuable resources for biochar production. On one hand, these solid wastes can be converted into biochar through pyrolysis, rather than being incinerated or mineralized, which can significantly reduce CO_2 emissions[9]. On the other hand, biochar can be utilized to capture CO_2, further contributing to the reduction of carbon emissions. Additionally, biochar can serve as soil amendment or fertilizer, helping to enhance carbon sequestration in the soil[10].

Textile dyeing sludge (TDS) is a typical kind of industrial sludge that generates approximately 21 million tons annually in China[11]. It is cost-effective and contains a higher concentration of toxic organic matter and active components compared to municipal sludge[12], making it a promising raw material for producing biochar[13]. Liu et al. [14] found the TDS biochar produced at 450 ℃ exhibited more

* Corresponding author at: Institute for Thermal Power Engineering, Zhejiang University, Hangzhou 310027, China.
E-mail address: hqx@zju.edu.cn (Q. Huang).

https://doi.org/10.1016/j.jcou.2025.103079
Received 31 December 2024; Received in revised form 10 March 2025; Accepted 4 April 2025
Available online 19 April 2025

developed pore structures than municipal sludge biochar. Additionally, the rich mineral composition of TDS biochar, including K, Fe and Ca [15], enhances its ability to chemisorb CO_2[16]. However, raw TDS has a high ash content, which reduces the micropore volume and results in an inadequately developed, clogged pore structure in the produced biochar, thus limiting its application[17].

Researchers have developed the co-pyrolysis method of sludge and biomass to improve the quality of biochar[18]. For instance, blending coffee grounds with sludge can significantly enhance the porosity and microporous volume of biochar[19]. Incorporating bamboo shoot shells helps maintain a relatively ordered carbon structure, achieving a CO_2 adsorption capacity of 3.53 mmol/g in the hybrid biochar[20]. Moreover, the alkali metals present in sludge promote lignin charring and pore development through a catalytic effect[21]. It has also been reported that the activation energy required during the co-pyrolysis of sludge and lignin is reduced, leading to lower energy requirements for the process[22]. Corncob is a significant agricultural biomass waste globally and is characterized by a higher carbon content and lower ash content compared to sludge[23]. Although corncob-based biochar mainly features a microporous structure, its relatively low density and limited diversity in pore structure restrict its broader applications[24]. Co-pyrolysis of TDS and corncob may integrate the distinct pore structures of TDS biochar and corncob biochar, offering a promising method to enhance the quality and stability of biochars for CO_2 capture. The alkali and alkaline earth metals in TDS function as catalyst, which can accelerate the thermal decomposition of organics and enhance the pore structure of the resulting biochar[25]. Zhu et al.[26] investigated the interaction mechanisms between TDS and the components of biomass—cellulose, hemicellulose, and lignin—and evaluated their influence on the three-phase products of co-pyrolysis. Huang et al.[27] observed that the inorganic compounds in TDS interacted with biomass volatiles, enhancing the intensity of pyrolysis. However, research on CO_2 adsorption performance of the hybrid biochar derived from TDS and corncob is still relatively limited.

In this study, the pore structures and CO_2 adsorption performances of biochars derived from TDS and corncob at various activation temperatures were analyzed. The objectives of this study are to: (i) investigate how the texture of biochar changes due to the synergistic effects of co-pyrolysis of TDS and corncob; (ii) determine the static and dynamic CO_2 adsorption capacities of different biochar samples; and (iii) evaluate the adsorption selectivity of CO_2/N_2 as well as the regeneration stability of the biochars. The findings will provide theoretical insights and practical guidance for the preparation of biochars from sludge and biomass, contributing methods for developing functional materials in the fields of adsorption and separation.

2. Material, methods and experimental section

2.1. Materials

The TDS was collected from a sludge incineration plant located in Zhejiang Province, China. Corncobs was obtained from a manufacturer in Jiangsu Province, China. K_2CO_3 was utilized as an activator and purchased from Beijing Standard Spectrum Testing Technology Co., ltd. The TDS was vacuum-dried at 105 °C for 24 h and then pulverized to a particle size fraction of less than 0.15 mm. A solvent-free, one-step method was applied to prepare biochar samples. 5 g of TDS powder, 5 g of corncob, and 10 g of K_2CO_3 were combined in a mortar, followed by thorough grinding and mixing. The mixture was then placed in a ceramic boat and heated in a N_2-purged tube furnace at temperatures of 600, 700, and 800 °C for 2 h, with at a flow rate of 100 mL/min and a heating rate of 10 °C/min. After the tube furnace cooled to room temperature, the biochar was removed and washed with 10 % HCl and then with deionized water until the pH was neutral. Finally, the samples were dried in an oven at 105 °C for 24 h. The hybrid biochar derived from TDS and corncob were designated as SCs. Specifically, the biochar prepared at different activation temperatures was labeled as SCT, where T represents the activation temperature. For comparison, TDS biochar and corncob-based biochar were also prepared and designated as ST and CT, respectively, while maintaining consistent preparation conditions with those used for SCs.

2.2. Characterization

Scanning electron microscopy (SEM, ZEISS Sigma 360) was employed to examine the surface morphology of biochar samples. The textural properties of biochar samples were determined by analyzing N_2 adsorption/desorption isotherms at 77 K. The specific surface area (S_{BET}) was calculated using the Brunauer-Emmett-Teller (BET) method, while the micropore volume (V_M) and specific surface area (S_M) were assessed using the t-Plot method. The total pore volume (V_T) was determined at a P/P_0 value of 0.99 from the adsorption isotherms. The pore size distribution (PSD) was obtained using the non-local density functional theory (NLDFT) method. Additionally, the ultra-micropore (<0.7 nm) specific surface area (S_{UM}) and ultra-micropore volume (V_{UM}) were analyzed using the cumulative pore volume method via the NLDFT method[28]. The particle size of biochar was measured using a particle size analyzer (Malvern Mastersizer 2000). Fourier transform infrared spectroscopy (FTIR, Scientific Nicolet iS20, Thermo Fisher, USA) was used to analyze functional groups. The X-ray diffraction (XRD) patterns of biochar were recorded with an X-ray diffractometer (Xpert 3). A Raman spectroscopy (LabRAM HR Evolution, HORIBA, JPN) was employed to investigate the chemical structure of biochar, using a light source with a wavelength of 532 nm. X-ray photoelectron spectroscopy (XPS, Thermo Scientific K-Alpha) was utilized to analyze the different types and distribution of surface functional groups. The ultimate analysis of raw materials and biochar was conducted using a Thermo Fisher Scientific Flash 2000 CHNS-O analyzer.

A thermogravimetric analyzer (TG209F3, NETZSCH) was employed to investigate the characteristics of mono-pyrolysis and co-pyrolysis of TDS and corncob. The thermal decomposition processes of corncob and TDS were anlyzed at a heating rate of 10 $K{\cdot}min^{-1}$ in N_2 using thermogravimetry (TG) and differential thermogravimetry (DTG) curves.

The thermal stabilities in N_2 and thermal oxidation resistance of the biochar samples were evaluated with the TG209F3. Graphite, which is known as the most stable carbonaceous material, served as a reference for assessing thermal oxidation resistance[29]. As shown in Eq. (1), the indicator R_{50} was utilized to evaluate the oxidation resistance of the biochar samples[30].

$$R_{50} = \frac{T_{50,biochar}}{T_{50,graphite}} \quad (1)$$

where $T_{50,\ biochar}$ refers to the temperature at which 50 % of the mass of biochar samples is oxidized, ℃; $T_{50,\ graphite}$ denotes the temperature at which 50 % of the mass of graphite is oxidized, ℃.

2.3. CO_2 adsorption experiment

The static CO_2 adsorption tests were conducted using the IGA-100C instrument. Before the tests, approximately 30 mg of the biochar sample was heated to 200 °C under high vacuum to remove contaminants and moisture. After cooling the sample to the experimental temperatures of 25, 50, and 60 °C, CO_2 was introduced into the chamber. The corresponding adsorption isotherms were generated by recording the mass change during the adsorption period at 2-second intervals.

The CO_2 dynamic adsorption experiments were carried out at 35 °C and 60 °C using a thermogravimetric analyzer (TGA55, TA). The experiments conducted at 35 °C were designated as SCT-35, while those at 60 °C were labeled SCT-60. Prior to testing, the biochar samples were dried at 105 °C for 3 h and then transferred to the TGA55. In a representative experiment, approximately 8 mg of biochar was placed in an

Table 1
Basic physiochemical properties of TDS and corncob.

Sample	Proximate analysis (wt%)				Ultimate analysis (wt%)					HHV^{d} (kJ/kg)
	M^{ar}	A^{d}	V^{d}	FC^{d}	C^{d}	H^{d}	N^{d}	S^{d}	O^{a}	
TDS	75.0	44.26	42.52	7.58	20.31	3.66	1.01	3.50	21.63	9642
Corncob	1.79	1.06	18.82	18.33	45.58	5.41	0.39	1.22	44.55	18021

ar, as received; d, dry basis; a, calculated by the difference.

Table 2
Ash composition of TDS.

Sample	SiO_2	Al_2O_3	Fe_2O_3	CaO	MgO	K_2O	Na_2O	Others
TDS	20.96	40.59	29.4	2.58	1.76	0.31	3.68	0.72

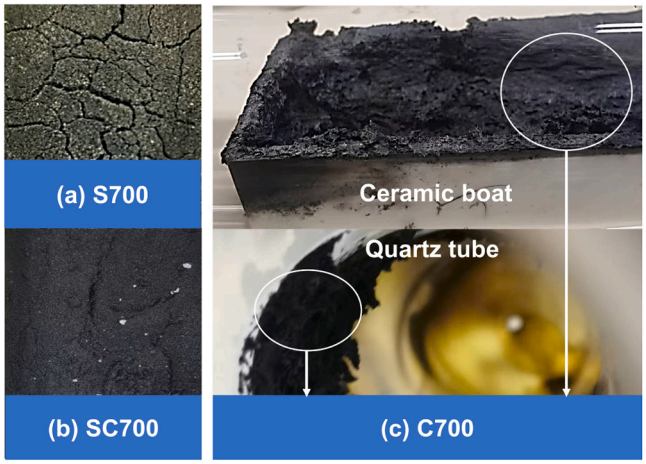

Fig. 1. Actual pictures of (a) S700, (b) SC700, (c) C700.

alumina crucible purged with 100 mL/min N_2 for 1 h. Then the N_2 flow was replaced with an equivalent flow of CO_2. The adsorption process was maintained at 35 °C and 60 °C for 40 mins, respectively.

The cyclic adsorption-desorption performance of biochar was evaluated by conducting ten static adsorption experiments using the IGA-100C, with a regeneration temperature set at 100 °C. The SC700 after 10 adsorption-desorption cycles was designated as SC700–10 used.

The *in situ* diffuse reflectance infrared Fourier transform (DRIFT) spectroscopy (Nicolet iS50) was employed to assess the changes in functional groups on SC700 surface during CO_2 adsorption. The adsorption experiment lasted for 40 mins at 35 °C, and the spectra were collected over the range of 4000–600 cm^{-1}.

3. Results and discussion

3.1. Experimental phenomena

The ultimate and proximate analyses, along with the higher heating values (HHVs) of TDS and corncob, are presented in Table 1. The elemental composition of TDS ash was analyzed and converted into oxide forms, as presented in Table 2. TDS contained a significantly higher amount of ash and a lower carbon content compared to corncob. As shown in Fig. 1 **(a)**, S700 displayed a grey-green coloration, which can be primarily attributed to the substantial presence of inorganic salts in TDS. In Fig. 1 **(c)**, the corncob and K_2CO_3 reacted vigorously during the chemical activation process, leading to coking, blistering, and a significant amount of biochar adhering to the walls of the quartz tube. In contrast, the co-pyrolysis activation reaction was relatively mild, resulting in a uniform hybrid biochar that is suitable for market applications.

3.2. Pyrolysis characterization

As shown in Fig. 2 (a), the mono-pyrolysis of TDS generated fewer volatiles than corncob, and could be dived into four distinct stages: (i) the removal of free water at temperatures ranging from 35 to 121 °C; (ii) the cracking reactions of cellulose, hemicellulose, and unstable proteins occurring in the 121–380 °C range; (iii) the pyrolysis of heavy molecular substances such as fats, macromolecular proteins, and lignin at temperatures between 380 and 635 °C; and (iv) the decomposition of inorganic salts in the 635–900 °C range, during which porous biochar was gradually formed[31]. The TG/DTG curves of the co-pyrolysis of TDS and corncob were situated between those of the mono-pyrolysis of TDS and corncob. SC-exp represented the experimental TG/DTG curves of the co-pyrolysis for TDS and corncob, while SC-cal represented the

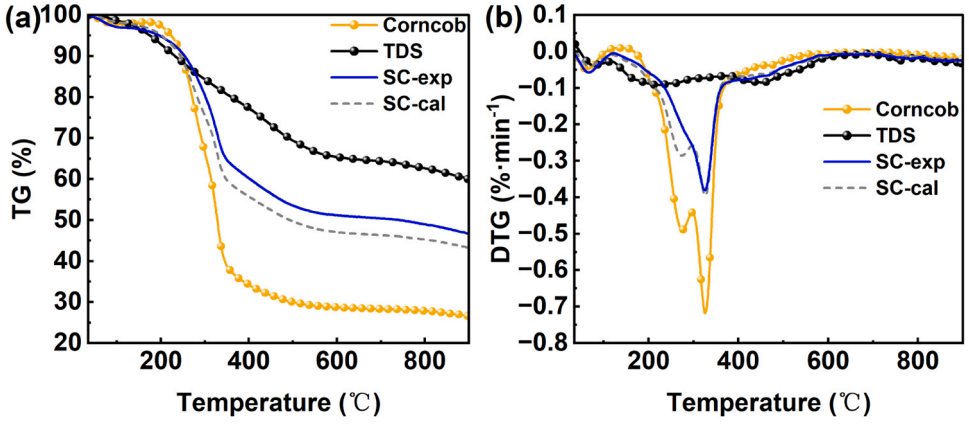

Fig. 2. (a) TG and (b) DTG curves of TDS and corncob pyrolysis.

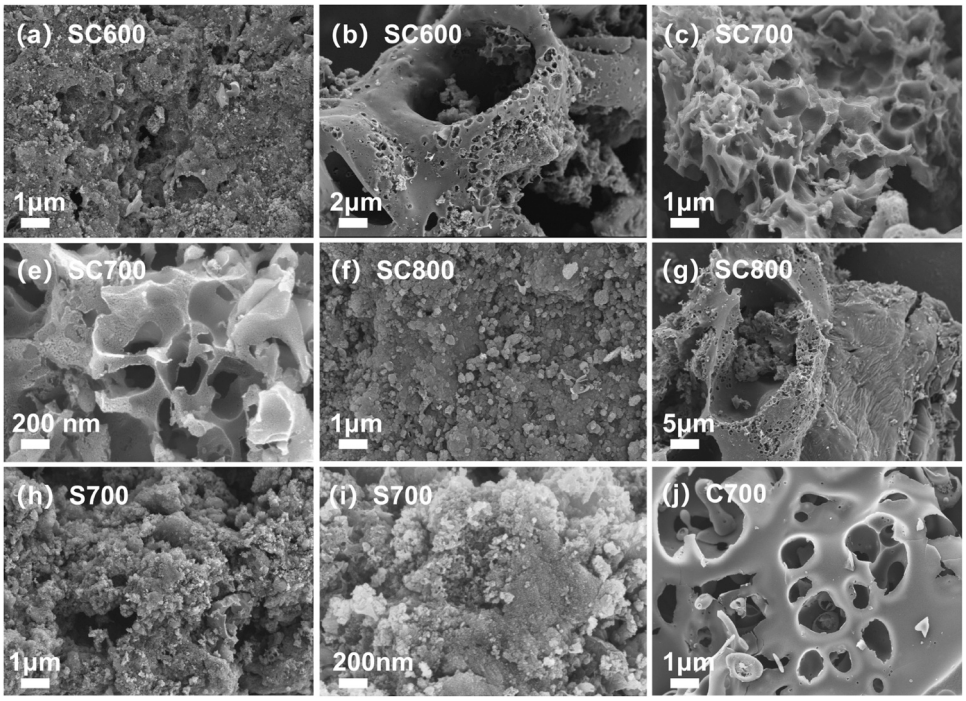

Fig. 3. SEM images of (a-b) SC600, (c-d) SC700, (f-g) SC800, (h-i) S700 and (j) C700.

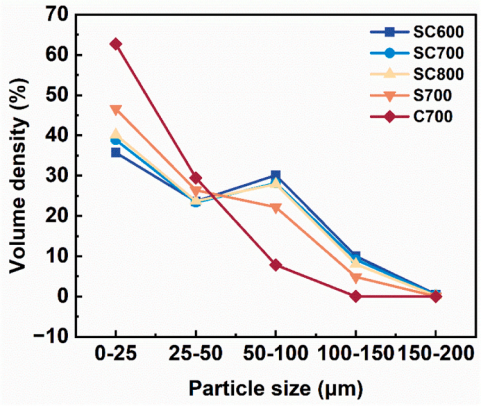

Fig. 4. Particle size distribution of the biochars.

calculated TG/DTG curves. In Fig. 2 (a), the SC-exp curve closely aligned with SC-cal curve at the beginning. However, once the temperature exceeded 250 °C, the SC-exp curve lagged behind the SC-cal curve, resulting in a final residue rate for the SC-exp curve that was higher than that of the SC-cal curve, with a deviation of 3.44 %. This indicates that synergistic effects occurred during co-pyrolysis, leading to an increased biochar yield. This enhancement is attributed to the interaction between organic matter in corncob and alkali and alkaline earth metals in TDS, such as magnesium (Mg), which can improve the dehydration reaction during pyrolysis and increase biochar yield[32,33]. Furthermore, the presence of alkali and alkaline earth metals in TDS contribute to the development of pores[21]. As illustrated in Fig. 2 (b), SC-exp curve lagged behind the SC-cal curve within the temperature range of 172–297 °C. As the reaction proceeded, the corncob released more heat and volatiles between 297 and 576 °C, which intensified the pyrolysis intensity of TDS[34]. This process led to an almost complete overlap of the DTG curves for SC-exp and SC-cal. These observations are consistent with the findings reported by Deng et al.[35].

3.3. Characteristics of biochar

3.3.1. SEM and particle size analysis

Fig. 3 illustrates the SEM images of all biochar samples. The surface morphology of S700 was complex, featuring loose and irregularly distributed pores. In contrast, the surface morphologies of SCs were relatively simple. Among the SCs, SC600 exhibited a layered structure with a sparse distribution of pores, while SC800 displayed a microcrystalline graphite structure with a negligible pore system. This difference is attributed to the ideal formation of biochar structures, where the skeletal carbon transitions from amorphous aromatic carbon to conjugated aromatic carbon, and ultimately to graphitic carbon as pyrolysis temperatures increase[36]. During thermal decomposition, the growth of turbostratic crystallites randomly creates 'gaps' that serve as pores of various sizes. Micropores can form from the voids between hexagonal planes[37]. That is why SC800 exhibited a higher S_M value compared to SC700. SC700 featured a microscopic honeycomb structure similar to that of C700. Among the SCs, SC700 had the most highly developed porous structure, indicating that 700 °C is the best temperature for K_2CO_3 activation to create the optimal pore structure. During the K_2CO_3 activation process, K_2CO_3 reacts with carbon to produce CO_2, CO, and metallic potassium (Eqs. (2–6))[38]. These substances help form a porous structure. The potassium ions (K^+) then penetrate the carbonized surface, causing the lattice to expand and promoting the growth of micropores (as shown in Eqs. (5–6))[39].

$$K_2CO_3 \rightarrow K_2O + CO_2 \quad (2)$$

$$K_2CO_3 + C \rightarrow K_2O + 2CO \quad (3)$$

$$2K + CO_2 \rightarrow K_2O + CO \quad (4)$$

$$K_2CO_3 + 2C \rightarrow 2K + 3CO \quad (5)$$

$$C + K_2O \rightarrow 2K + CO \quad (6)$$

The particle size distributions of the biochars are illustrated in Fig. 4. The particle size distributions of SCs and S700 showed similar characteristics, with the majority of particles concentrated in the ranges of

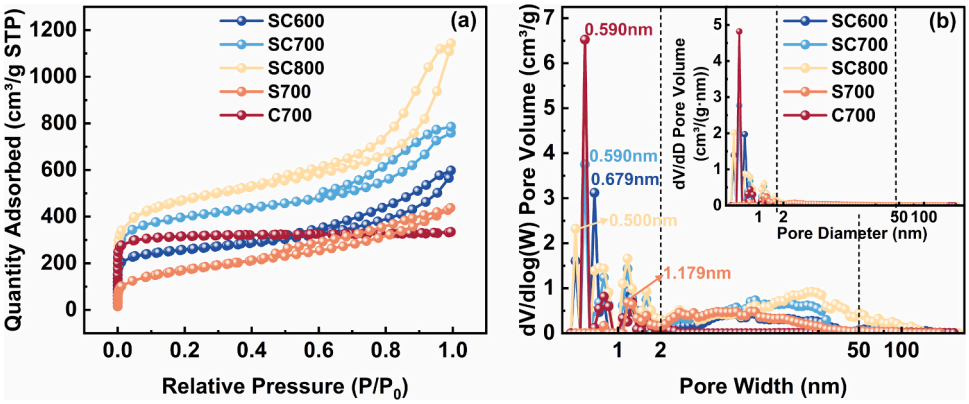

Fig. 5. (a) N_2 adsorption-desorption isotherms and (b) NLDFT pore size distributions of all biochar samples.

Table 3
Pore structure characteristics of different biochar samples.

Biochar	S_{BET} (m^2/g)	S_M (m^2/g)	S_{UM} (m^2/g)	V_T (cm^3/g)	V_M (cm^3/g)	V_{UM} (cm^3/g)	D_A (nm)
SC600	957.05	600.09	458.98	0.93	0.24	0.14	3.87
SC700	1442.42	928.22	544.38	1.22	0.39	0.16	3.37
SC800	1700.26	938.08	404.23	1.77	0.39	0.11	4.16
S700	603.98	112.13	0	0.68	0.05	0.02	4.48
C700	1239.42	1017.72	886.05	0.52	0.39	0.26	1.67

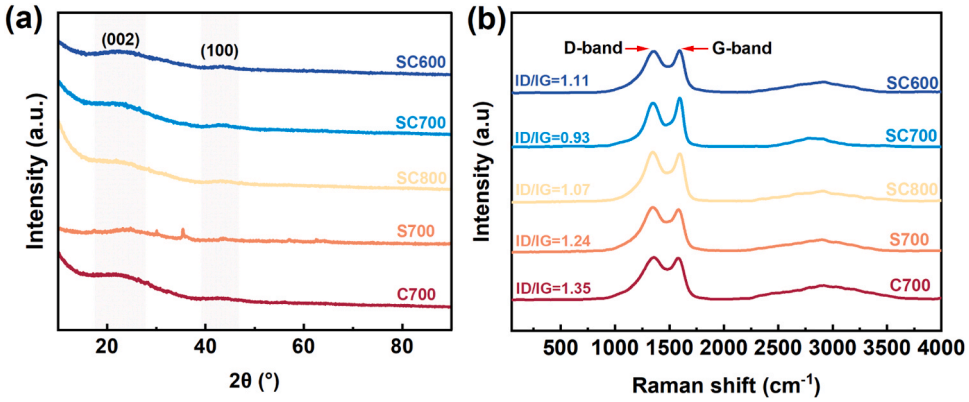

Fig. 6. (a) XRD patterns and (b) Raman spectra of carbons from biochars.

0–25 μm and 50–100 μm. In contrast, the particle size of C700 was primarily concentrated within the range of 0–25 μm.

3.3.2. *Specific surface area and pore size distribution*

As illustrated in Fig. 5 (a), C700 exhibited a typical type I N_2 adsorption isotherm, reaching saturation rapidly when the relative pressure (P/P_o) exceeded 0.01. In contrast, the N_2 adsorption isotherms of S700 and SCs displayed a combination of type I and type IV isotherms. At low relative pressures ($P/P_o < 0.01$), there was a sharp increase in N_2 uptake, indicating the filling of micropores. The gradual rise between $P/P_o = 0.45$ and 0.99, accompanied by a hysteresis loop, indicated capillary condensation in mesopores. The H_4-type hysteresis loop shows that the adsorption of the desorbed branch is greater than that of the adsorbed branch at the same relative pressure. This phenomenon is typically observed in adsorbents with both micro- and mesopores, as well as in materials that contain narrow slit pores, such as biochars and molecular sieves[40]. Fig. 5 (b) presents the PSD characteristic curves of all biochar samples. Evidently, C700 possessed a purely microporous structure, whereas the SCs and S700 exhibited a hierarchical porous structure consisting of both micropores and mesopores. The presence of mesopores facilitates sufficient mass transfer channels during the dynamic adsorption process, enhancing CO_2 capture[41]. Additionally, as the pyrolysis temperature increased from 600 to 800 °C, the pore diameter corresponding to the largest fraction of the pore volume in SCs, decreased from 0.679 to 0.500 nm. Given that the kinetic diameter of CO_2 is 0.33 nm, ultra-micropores represent the optimal pore size for CO_2 adsorption[42]. This indicates that SCs possess the necessary pore structure for significant CO_2 adsorption. In contrast, S700 showed a limited amount of micropores and a significant microporous distribution at 1.179 nm, lacking ultra-micropores.

The pore structure parameters of SCs, S700 and C700, including S_{BET}, V_T, S_M, V_M, S_{UM}, V_{UM}, and average pore diameter (D_A), are all summarized in Table 3. Among these samples, S700 exhibited the lowest values for S_{BET} and S_M, with its S_{UM} value reaching zero. This suggests that the co-pyrolysis of TDS and corncob promotes the development of micropores and ultra-micropores. Among the SCs, SC800 exhibited the highest values for S_{BET} and S_M, followed by SC700 and SC600. This trend indicates the S_{BET} and S_M values of SCs increase as the activation temperature rises. However, it is noteworthy that the S_{UM} and V_{UM} values for SC700 were higher than those for SC600 and SC800, indicating that 700 °C is optimal for generating ultra-micropores through K_2CO_3 activation.

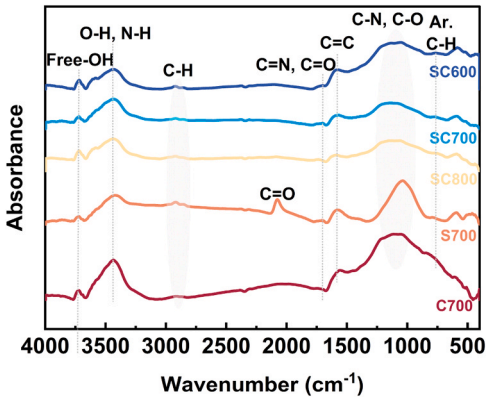

Fig. 7. FTIR spectra for the biochars.

3.3.3. XRD and Raman analysis

Fig. 6 (a) shows characteristic features of amorphous carbon, indicated by broad (002) and (100) diffraction peaks at 2θ = 23° and 43°, respectively[43]. The (002) crystalline reflection corresponds to graphene sheets arranged in a turbostratic manner, stacked along the z-axis. The (100) crystalline plane is associated with the lateral expansion of graphene sheets[37]. The SCs and C700 exhibited enhanced low-angle scattering intensity compared to S700, which aligns with the greater porosity observed in Fig. 3[44]. This change suggests a higher presence of defects and structural disorder, likely caused by the degradation of graphitic domains and alterations in the turbostratic arrangements of the carbon layers[37].

The Raman spectra presented in Fig. 6 (b) showed distinct D and G bands, corresponding to disordered carbon structures/graphite phase defects and ordered graphitic domains, respectively[45]. The relative

Table 4
Summary of C/N/O elemental contents and semi-quantitative results of different nitrogen functional groups of the biochar samples.

Biochar	Atomic %			N %		
	C	N	O	N-6	N-5	N-Q
SC600	83.46	1.59	14.95	23.22	28.19	48.59
SC700	87.13	1.03	11.84	40.58	36.05	23.37
SC800	90.04	0.81	9.15	19.96	14.47	65.57
S700	72.8	3.09	24.11	44.18	24.42	31.4
C700	90.67	0.78	8.54	38.14	28.63	33.23

Table 5
Ultimate analysis results of SCs, S700, and C700 (Mass, %).

Biochar	N	C	H	S	O	O/C	H/C
SC600	0.527	63.395	0.972	3.913	11.42	0.180	0.015
SC700	0.381	75.316	0.650	3.981	8.105	0.108	0.009
SC800	0.350	73.855	0.594	3.293	6.12	0.083	0.008
S700	0.801	28.232	1.252	17.369	16.38	0.580	0.044
C700	0.044	73.727	0.495	0	5.63	0.076	0.007

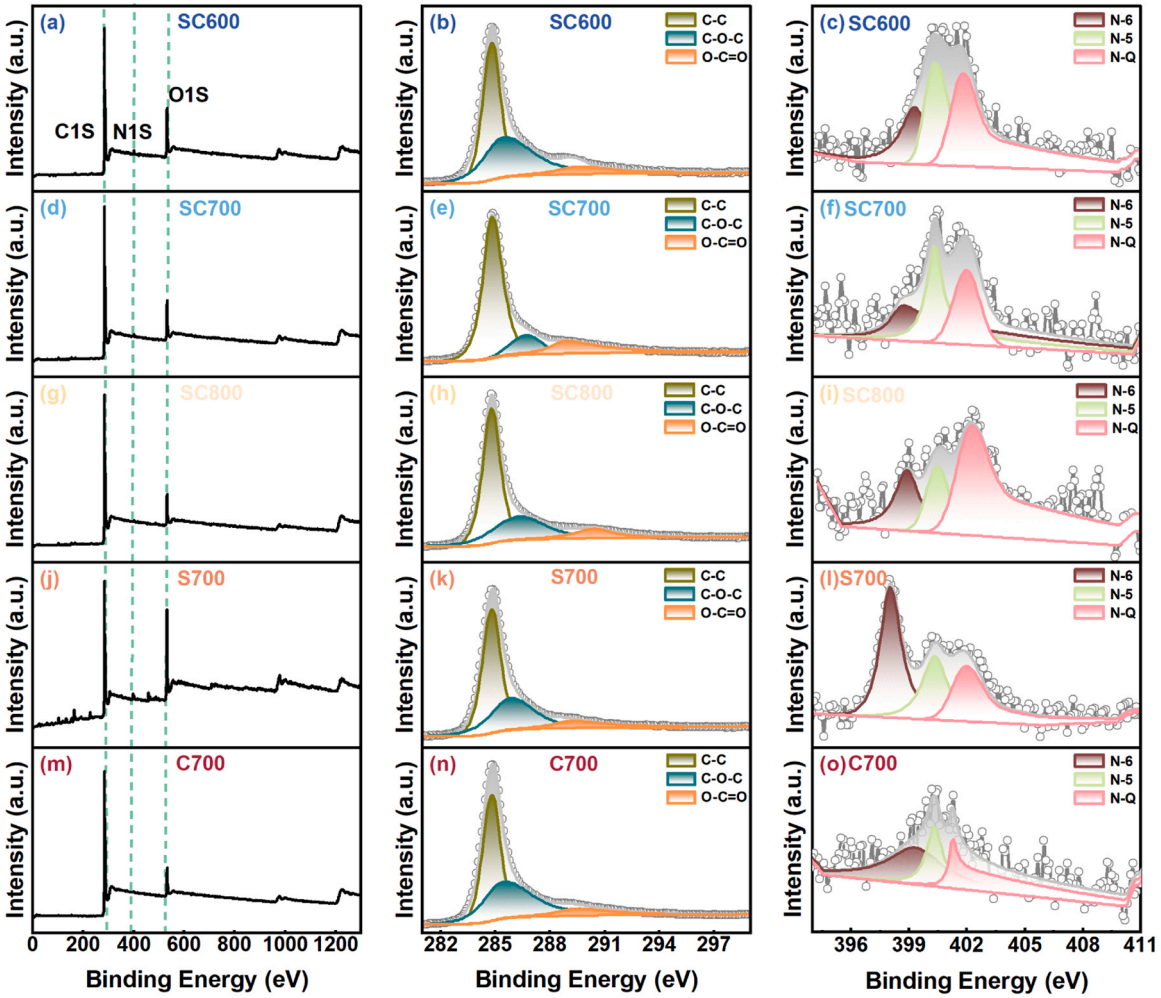

Fig. 8. XPS spectra, C1s and N1s XPS spectra of the biochar samples.

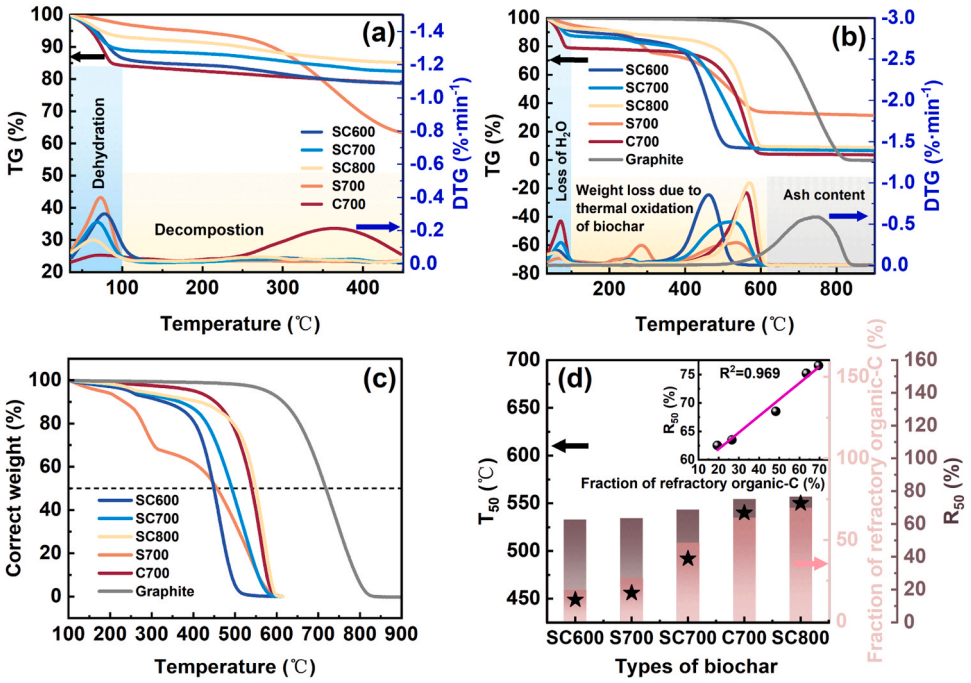

Fig. 9. Thermal stability (a), thermal oxidation resistance (b), water and ash content-corrected TG curves (c) and correlation analysis between R_{50} and the fraction of refractory organic-C (d) of biochar samples.

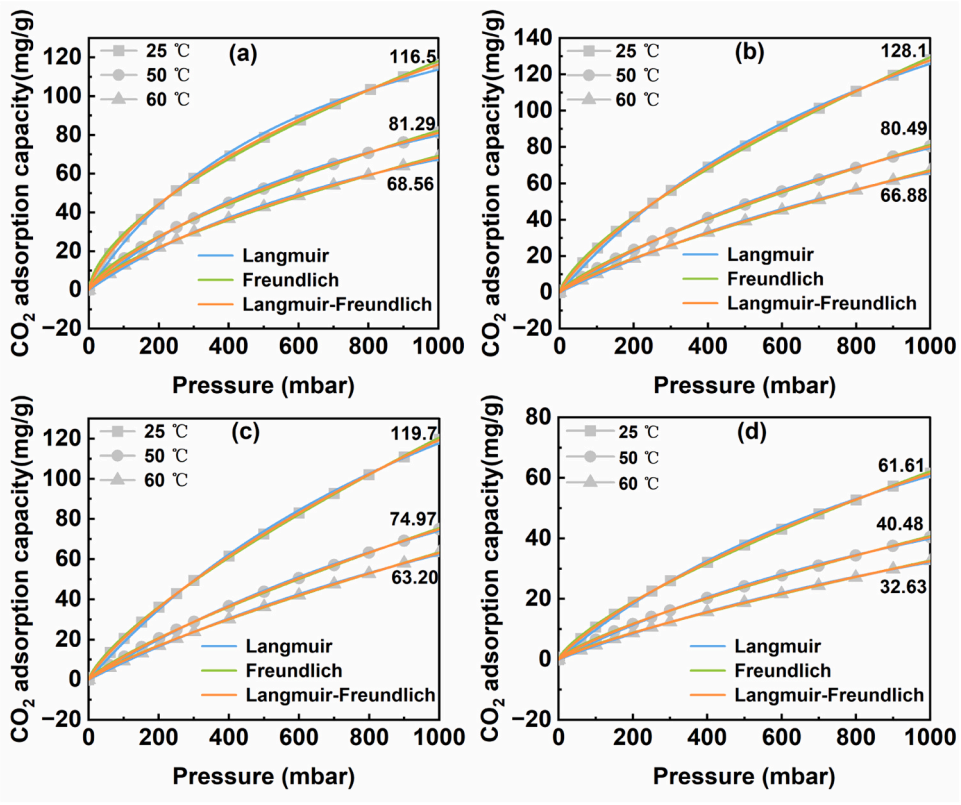

Fig. 10. CO_2 adsorption capacities of (a) SC600, (b) SC700, (c) SC800, and (d) S700 at different adsorption temperatures.

intensity ratio of D to G bands (I_D/I_G) serves as a quantitative measure of graphitic ordering where lower values indicating higher crystallinity. The I_D/I_G values for S700 and C700 (1.24 and 1.35, respectively) were higher than those of SCs, suggesting a greater presence of defects in the carbon structure. Consequently, the co-pyrolysis method can enhance the degree of carbon graphitization to some extent. Notably, the I_D/I_G ratio of SCs decreased from 600 to 700 °C, followed by an increase between 700 and 800 °C. These findings are consistent with the results obtained from XRD analysis. While the microcrystalline graphite structure was observed in SC800 in Fig. 3 (f), the non-uniform growth of

Table 6
Values of the χ^2 error of CO_2 adsorption isotherms for each analyzed model.

Biochar	Langmuir	Freundlich	Redlich-Peterson	Radke-Prausnitz	Toth	Langmuir-Freundlich
Temperature 25 °C						
SC600	1.113917	0.411517	**0.002912**	0.002936	0.003834	0.012286
SC700	0.686018	0.295330	0.000495	0.000494	**0.000123**	0.004392
SC800	0.531727	0.173809	**0.000379**	0.000381	0.000626	0.005014
S700	0.251838	0.136506	**0.000423**	0.000441	0.000979	0.005032
Temperature 50 °C						
SC600	0.461271	0.253858	0.001767	0.001768	**0.000810**	0.002570
SC700	0.250988	0.131033	0.001813	0.001814	**0.001094**	0.000827
SC800	0.197612	0.071192	0.001396	0.001396	**0.000960**	0.000578
S700	0.161389	0.043284	0.001240	0.001240	**0.000972**	0.001009
Temperature 60 °C						
SC600	0.336915	0.166568	0.001935	0.001934	**0.001653**	0.003735
SC700	0.196320	0.072781	0.001790	0.001791	**0.001455**	0.001598
SC800	0.203522	0.028455	0.003057	0.003057	0.002931	**0.001773**
S700	0.079742	0.033048	**0.002430**	0.002436	0.002585	0.003950

graphene sheets[45], changes in the turbostratic arrangements of the carbon layers and an increase in micropore generation contributed to a greater presence of defects and disorder. Shafawi et al.[46] reported that as the pyrolysis temperature increases, the symmetry of carbon atoms is disrupted, leading to the formation of defects in biochar. Similar observations were reported in the studies conducted by Jia et al.[47] and Liu et al.[48]. Although SC800 exhibited more defects than SC700 with an I_D/I_G ratio of 1.07, the analysis of pore structures revealed that SC700 possessed greater S_{UM} and V_{UM} than SC800, which is a more critical property for CO_2 capture.

3.3.4. FTIR analysis

The FTIR spectra reveals various functional groups present on the surfaces of the biochars, which evolve with increasing activation temperatures (as shown in Fig. 7). It can be observed that SCs, S700 and C700 showed similar peaks, with the exception that S700 had an additional C═O peak at 2080 cm^{-1}[49]. All the biochars exhibited some similar peaks at 3725, 3437, 2929 and 2852 cm^{-1}. These peaks could be ascribed to free–OH[50], phenol O–H, asymmetric and symmetric C–H stretching vibrations in aliphatic CH, CH_2, and CH_3, respectively[51]. The intensity of phenol O–H peak tended to decrease with increasing activation temperature, indicating a reduction in hydroxyl groups or absorbed water[52]. In the range of 1745–1586 cm^{-1}, there was a strong band attributed to oxime C═N–OH, pyridine C═N, and C═O stretching vibrations. The bands around 1564 cm^{-1} could be assigned to C═C[53], indicating that aromatic structures were a significant component of the activated carbons' chemical makeup[52]. Notably, the exact position of this peak shifted slightly to higher wavenumbers, moving from 1594 cm^{-1} in SC600 to 1604 cm^{-1} in SC800. The peak at 1070 cm^{-1} was associated with the C–N stretching vibrations of amide groups[53], while the region between 1100 and 1000 cm^{-1} likely corresponded to C–O stretching[51]. The intensity of main oxygen-containing functional groups such as phenol O–H (3437 cm^{-1}), C═O (1745–1586 cm^{-1}) and C–O (1100–1000 cm^{-1}) decreased as the pyrolysis temperature increased. In contrast, the intensity of aromatic C–H (750 cm^{-1}) increased with rising pyrolysis temperatures[54]. This trend indicated a greater presence of condensed polyaromatic sheets, which are more resistant to biological and thermochemical degradation, thereby demonstrating high stability[55].

3.3.5. XPS analysis

The porous structure and surface functional groups are two crucial factors that influence the CO_2 adsorption performance of biochar. Fig. 8 presents the XPS spectra of all biochar samples. Table 4 provides the semi-quantitative results of the fitted C/N/O elemental content and various nitrogen functional groups. Since TDS and corncob were nitrogenous raw materials, all the biochar samples contained nitrogen. Among these samples, S700 exhibited the highest N content (3.09 %), while C700 had the lowest at 0.78 %. The N content in SCs ranged from 0.81 % to 1.59 %. Moreover, the N content in SCs decreased gradually as the activation temperature increased, aligning with the research findings of Lu et al.[56]. The nitrogen functional groups are classified into three types: pyridine nitrogen (N-6), pyrrolic nitrogen (N-5), and quaternary nitrogen (N-Q)[57]. S700 had the highest content of N-6 (44.18 %), followed by SC700 (40.58 %), C700 (38.14 %), SC600 (23.22 %), and SC800 (19.96 %). N-6 acts as Lewis bases, which interacts with the electron-deficient carbon in CO_2 during the adsorption process[58]. In contrast, N-5 and N-Q function as N-type dopants rather than Lewis bases. These groups can enhance the surface electrical current density, indirectly improve the adhesion of CO_2[59].

3.3.6. Ultimate analyses of biochars

The ultimate analysis results of SCs, along with S700, and C700, are presented in Table 5. As the pyrolysis temperature increased, the H/C and O/C ratios of the SCs decreased, which was consistent with FTIR analysis. This change is attributed to the breakdown of weaker bonds (e.g., alky-aryl ether bonds) and an increase in the condensation of aromatic hydrocarbons in the biochar structure[55]. The H/C ratios of SCs ranged from 0.007 to 0.044, while the O/C ratios varied from 0.076 to 0.580. According to EBC guidelines, biochar is considered stable if its H/C ratio is below 0.7 and its O/C ratio is under 0.4[60]. Therefore, SCs and C700 can be utilized for carbon sequestration in soil, serving as materials for long-term CO_2 storage.

3.3.7. Thermal stability and thermal oxidation resistance

The thermal stability of biochar is essential for its application in high-temperature environments and regeneration processes. Previous studies have shown that the highest temperature required for pre-combustion, oxy-combustion, and post-combustion CO_2 capture techniques is 450 °C[42]. Therefore, the thermal stability of biochar at this temperature was evaluated. As illustrated in Fig. 9 **(a)**, the biochar released free water at temperatures below 100 °C, and its carbon skeletons decomposed between 100 and 450 °C. SC700 exhibited the highest thermal stability, with a carbon skeleton loss of 6.71 %. In comparison, SC800 showed a maximum loss of only 8.10 %. Conversely, the carbon skeleton mass loss for S700 and C700 were significantly higher, at 33.75 % and 5.59 %, respectively. This indicates that the addition of corncob enhances the thermal stability of the SCs. Overall, all biochar samples exhibited a carbon skeleton loss of less than 8.10 %, demonstrating good thermal stabilities. This performance is superior to that of alkali metal-doped carbon materials, which typically exhibited a weight loss of approximately 10 %[61].

The thermal oxidation resistance of biochar significantly influences its sustainable application potential and carbon sequestration capacity in soil. The original thermogram (Fig. 9 (b)) was corrected for water and ash content[30], resulting in Fig. 9 (c). Fig. 9 (d) illustrates the

Table 7
The isotherm constants of the analyzed models of SCs and S700.

Biochar	Temperature (°C)	Langmuir model		Freundlich model		Redlich-Peterson model			Radke-Prausnitz model			Toth model			Langmuir-Freundlich model		
		K_L	q_m	K_F	n_F	a_{RP}	K_{RP}	β_{RP}	q_m	K_{RPr}	ε_{RPr}	q_m	K_T	n_T	K_S	q_m	n_S
SC600	25	0.0016	180.6	1.5969	1.6018	0.0640	0.5311	0.5816	8.3040	0.0639	0.5816	1146	0.0007	0.3350	0.0004	363.7	0.7599
	50	0.0011	148.6	0.6788	1.4370	0.0443	0.2579	0.5634	5.8294	0.0442	0.5636	960	0.0003	0.3770	0.0003	284.7	0.8203
	60	0.0010	136.6	0.4621	1.3765	0.0464	0.1962	0.5345	4.2295	0.0464	0.5346	1193	0.0002	0.3627	0.0003	274.7	0.8346
SC700	25	0.0010	249.6	0.9129	1.3919	0.0517	0.3856	0.5298	7.4695	0.0516	0.5300	2382	0.0002	0.3488	0.0003	516.9	0.8253
	50	0.0007	194.7	0.3695	1.2790	0.0401	0.1848	0.5029	4.6009	0.0402	0.5026	2375	0.0001	0.3675	0.0002	399.6	0.8697
	60	0.0006	177.5	0.2621	1.2436	0.0517	0.1476	0.4562	2.8497	0.0518	0.4559	4434	0.0000	0.3273	0.0002	406.3	0.8749
SC800	25	0.0008	266.9	0.6342	1.3147	0.0613	0.3189	0.4781	5.1747	0.0617	0.4774	5119	0.0001	0.3171	0.0002	615.9	0.8435
	50	0.0005	209.5	0.2735	1.2277	0.0514	0.1594	0.4467	3.0989	0.0515	0.4465	6152	0.0000	0.3240	0.0001	486.4	0.8811
	60	0.0005	186.3	0.2140	1.2128	0.1192	0.1518	0.3569	1.2687	0.1198	0.3564	33545	0.0000	0.2458	0.0001	597.1	0.8690
S700	25	0.0008	132.4	0.3497	1.3313	0.0412	0.1581	0.5270	3.7489	0.0424	0.5239	1213	0.0001	0.3739	0.0002	264.8	0.8521
	50	0.0007	98.4	0.1834	1.2768	0.0716	0.1025	0.4432	1.4341	0.0714	0.4435	3412	0.0000	0.2934	0.0002	244.3	0.8535
	60	0.0005	94.6	0.1108	1.2137	0.0447	0.0654	0.4519	1.4143	0.0465	0.4479	2537	0.0000	0.3366	0.0001	216.5	0.8886

correlation analysis between R_{50} and the fraction of refractory organic carbon, which includes poly-condensed forms of lipids and aromatic carbon with a degradation range of 475–600 °C[60]. Notably, as the activation temperature increased, both the R_{50} values and the content of refractory organic carbon also rose. This is consistent with the conclusion in Fig. 7 that the intensity of Ar. C–H increases as the pyrolysis temperature rises. Additionally, the thermal oxidation resistance of the biochar showed a strong positive correlation with the refractory organic carbon content ($R^2 = 0.969$), aligning with the research findings of Xu et al.[29].

3.4. CO_2 adsorption behavior and mechanism

3.4.1. CO_2 adsorption isotherms

Fig. 10 presents the static CO_2 adsorption capabilities of SCs and S700. At 25 °C and 1 bar, SC700 exhibited the highest CO_2 adsorption capacity, reaching 128.1 mg/g, followed by SC800 (119.7 mg/g), SC600 (116.5 mg/g), and S700 (61.61 mg/g). The superior performance of SC700 can be attributed to its well-developed ultra-micropores structure and nitrogen functional groups, which provide abundant CO_2 adsorption sites. Interestingly, although SC700 contained a lower N-6 content compared to S700, its CO_2 adsorption capacity was more than double that of S700. This difference highlights the fact that at low temperatures, the CO_2 adsorption capacity is primarily influenced by the presence of ultra-micropores, as noted in the research by Li et al.[42]. At higher temperatures, chemisorption tends to dominate the adsorption [60]. However, it was observed that the CO_2 adsorption performance of the SCs decreased with rising temperatures. This decline is likely due to higher temperatures accelerating the Brownian motion of CO_2 molecules, which promotes their desorption[62]. These findings suggest that the adsorption mechanisms for the SCs and S700 are predominantly governed by physical adsorption.

To fit the CO_2 adsorption data, the two-parameters isotherm models (Langmuir and Freundlich) and three-parameters isotherm models (Redlich-Peterson, Radke-Prausnitz, Toth, and Langmuir-Freundlich) were employed. Detailed computational methods can be found in the research conducted by Serafin et al.[63]. Additionally, the analysis utilized 7 types of error functions: the coefficient of determination (R^2), the sum of the squares error (SSE), the sum of absolute errors (SAE), the gybrid fractional error function (HYBRID), the Marquardt's percent standard deviation (MPSD), the average relative error (ARE), and the chi-square test (χ^2). We also calculated the sum of normalized errors (SNE). The different parameters of all the analyzed models examined for SC600, SC700, SC800, and S700 were included in the adsorption isotherms section of the Supplementary Material. As shown in the Supplementary Material, the χ^2 error provided the lowest SNE values for most systems. Consequently, we selected it as the error function to evaluate the fit of the isothermal models to the experimental data.

Table 6 presents the χ^2 error values for the CO_2 adsorption isotherms analyzed using different models, while the corresponding isotherm constants are provided in Table 7. It is clear that the three-parameter models better fit the experimental data compared to the two-parameter models. Most of the Redlich-Peterson and Toth models displayed extremely low χ^2 errors, highlighted in bold, indicating that the CO_2 adsorption across the entire temperature and pressure range occurs via multilayer adsorption. Furthermore, as both the pyrolysis temperature and the adsorption temperature increased, the value of β_{RT} shifted from approaching 1 to approaching 0. This suggests that the Redlich-Peterson model tends to simplify to the Freundlich model when adsorbing high concentrations of CO_2. In the Toth models for all biochars, the values of n_T were not equal to 0 (0.335024–0.376986 for SC600, 0.327283–0.367510 for SC700, 0.245760–0.324047 for SC800, and 0.293374–0.373882 for S700), indicating that the biochar samples possess heterogeneous pore structures[64]. This finding aligns with the results obtained from Fig. 3 and Fig. 5. Additionally, it was observed that K_L and K_F decreased with increasing adsorption temperature, which

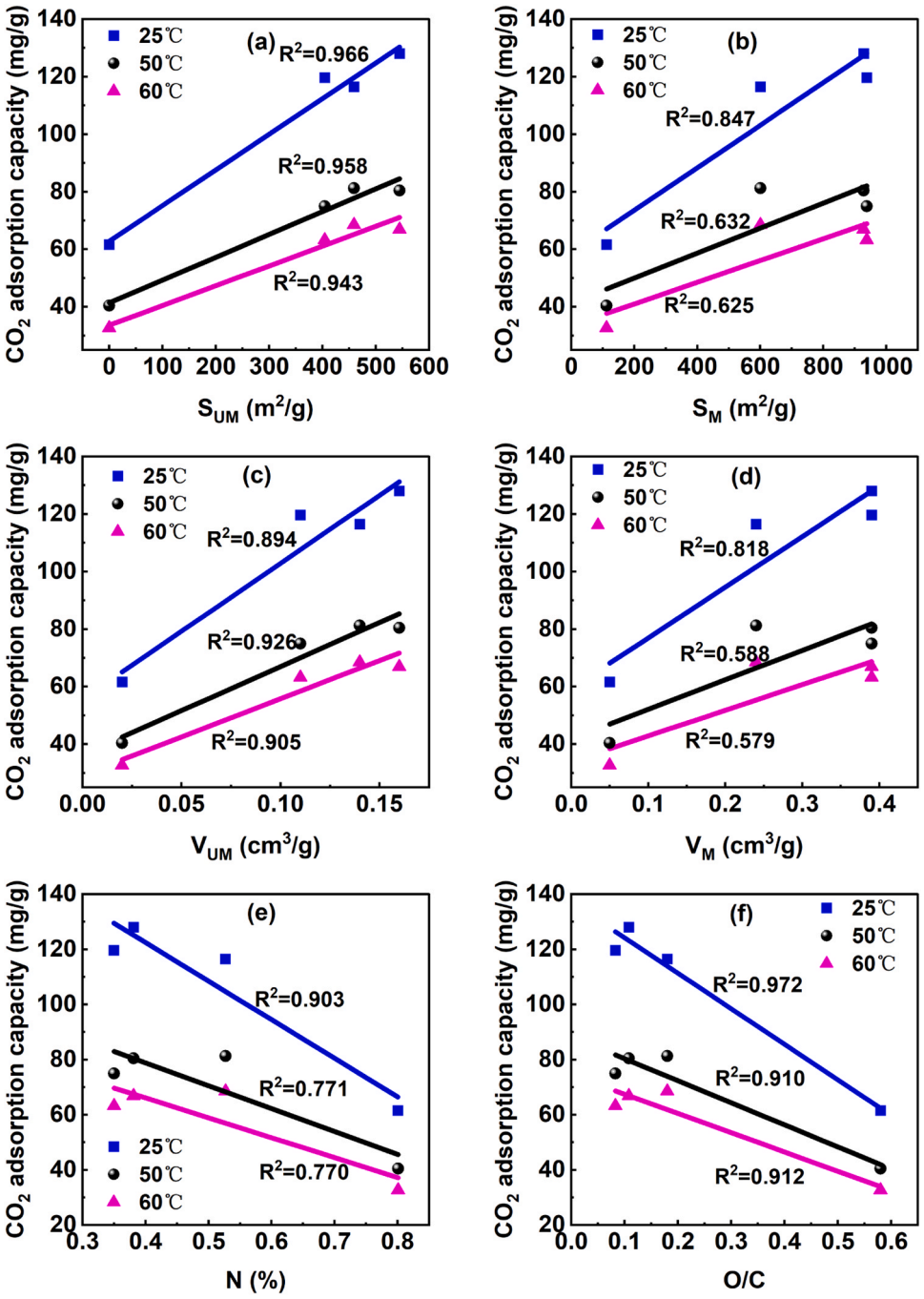

Fig. 11. Correlation analysis between CO_2 adsorption capacities and (a) S_{UM}, (b)V_M, (c) S_{UM}, (d) V_{UM}, (e) N content, and (f) O/C ratio at different temperatures.

suggests a physisorption behavior[65]. Furthermore, the values of n_F in the Freundlich model were all greater than 1, indicating that the primary CO_2 adsorption mechanism is physical adsorption[66].

As shown in Fig. 11, the correlation analysis was conducted to further investigate the impact of S_M, V_M, S_{UM}, V_{UM}, N content, and O/C ratio on the static adsorption performance of SCs and S700. At the same adsorption temperatures, the R^2 values of S_{UM} (0.943–0.966), V_{UM} (0.894–0.926), N content (0.770–0.903) and O/C ratio (0.910–0.972) were higher compared to S_M (0.625–0.847) and V_M (0.579–0.818). This indicates that the pore volume and pore area of ultra-micropores are more influential for the static adsorption of CO_2 than those of micropores. Additionally, the oxygen-containing and nitrogen-containing functional contribute to the chemical adsorption of CO_2.

The *in situ* DRIFT spectra ranging from 4000 to 550 cm^{-1} is presented in Fig. 12. The asymmetric stretching vibrations of CO_2 at 2343 and 2364 cm^{-1} remained stable throughout the adsorption process, confirming the dominance of physisorption via van der Waals interactions [23]. At the same time, a weak carbonates peak appeared at 1750 cm^{-1}, suggesting some degree of CO_2 chemisorption[67]. The presence of C-N bonds near 1520 cm^{-1} confirmed the formation of bonds between nitrogen atoms in the nitrogen-containing functional groups and carbon atoms derived from CO_2, providing direct evidence of the involvement of these groups in CO_2 chemisorption[68]. Additionally, two distinct bending vibrations at 669 and 721 cm^{-1} corresponded to the bending vibration of CO_2[69]. Four sharp and well-distinguished bands at 3599, 3627, 3705, and 3730 cm^{-1} were attributed to the combination bands of CO_2[68]. Altogether, these spectral characteristics illustrate the multi-modal adsorption behavior of CO_2 of biochars.

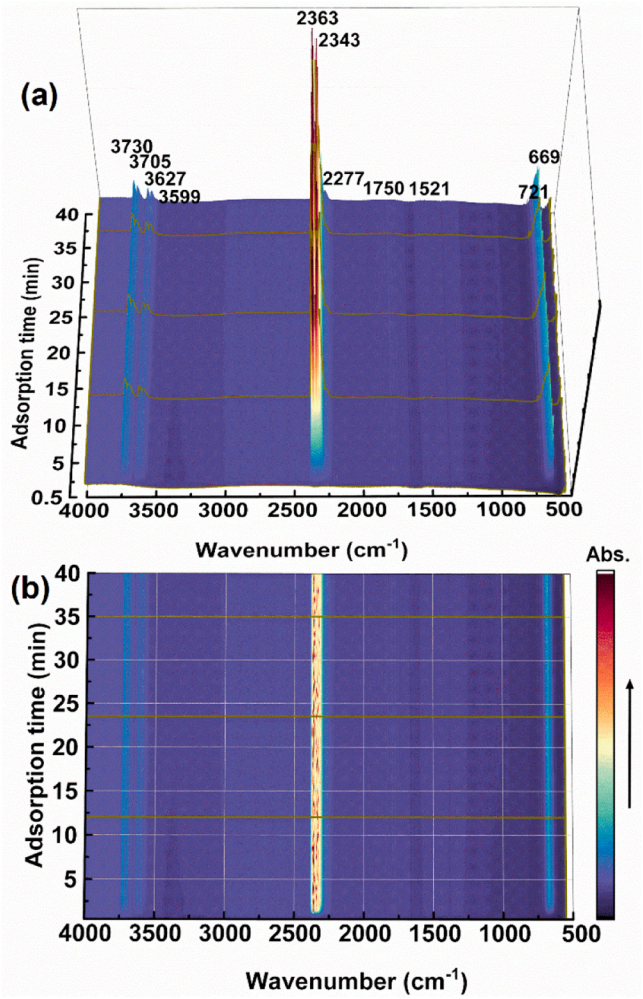

Fig. 12. *In situ* DRIFT spectra of adsorbed CO_2 by SC700 at 35 °C.

Fig. 13 (a-b) displays the SEM images of SC700 and SC700–10 used, respectively. After 10 cycles tests, it was obviously seen that the original pore structure partially collapsed and broke down, while the biochar structure remained relatively complete. The similar pore changes phenomenon was also observed by Gong et al.[70]. As depicted in Fig. 13 (c), the I_D/I_G value of SC700–10 used was higher than that of SC700. This can be attributed to the increased defects and disorder resulting from the changes in pore structure. The FTIR spectra of SC700 and SC700–10 used are presented in Fig. 13 (d). Compared to the FTIR spectra of SC700, SC700–10 used exhibited a stronger C–N stretching mode and weaker N–H, C–O, C═O stretching modes. The C–N bonds were formed by the combination of nitrogen atoms from the nitrogen-containing functional groups with carbon atoms from CO_2[68]. The N–H and oxygen functional groups were consumed during the CO_2 adsorption process[71].

3.4.2. *CO_2 adsorption kinetics*

Fig. 14 shows the dynamic CO_2 adsorption results of biochar samples. It is noteworthy that the dynamic adsorption capacities of SCs and S700 were lower than their static adsorption capacities. This difference is due to the relatively short residence time of CO_2 during dynamic adsorption. The dynamic adsorption capacities of S700 at 35 and 60 °C were nearly negligible. The observed weight loss was attributed to its limited ability to store CO_2. This occurs because the mobile phase of CO_2 carried away the CO_2 that was previously adsorbed before. In contrast, the adsorption capacities of SCs ranged from 37.18 to 43.19 mg/g at 35 °C, while SC700 exhibited the highest adsorption capacity. All the SCs reached adsorption equilibrium in approximately 6 mins. To further quantify the adsorption kinetic process, the Pseudo-first-order model, Pseudo-second-order model, and Avrami model were employed to fit the kinetic curves. Detailed mathematical descriptions can be found in the adsorption kinetics models section of the Supplementary Material. As shown in Table 8, the R^2 values for the curves generated by the Avrami model ranged from 0.990 to 0.994, which were higher than those of Pseudo-first-order model (0.948–0.963) and Pseudo-second-order model (0.839–0.864). This indicates that the Avrami model is the most suitable model for fitting the CO_2 adsorption kinetics in this study.

To identify the factors influencing the CO_2 dynamic adsorption

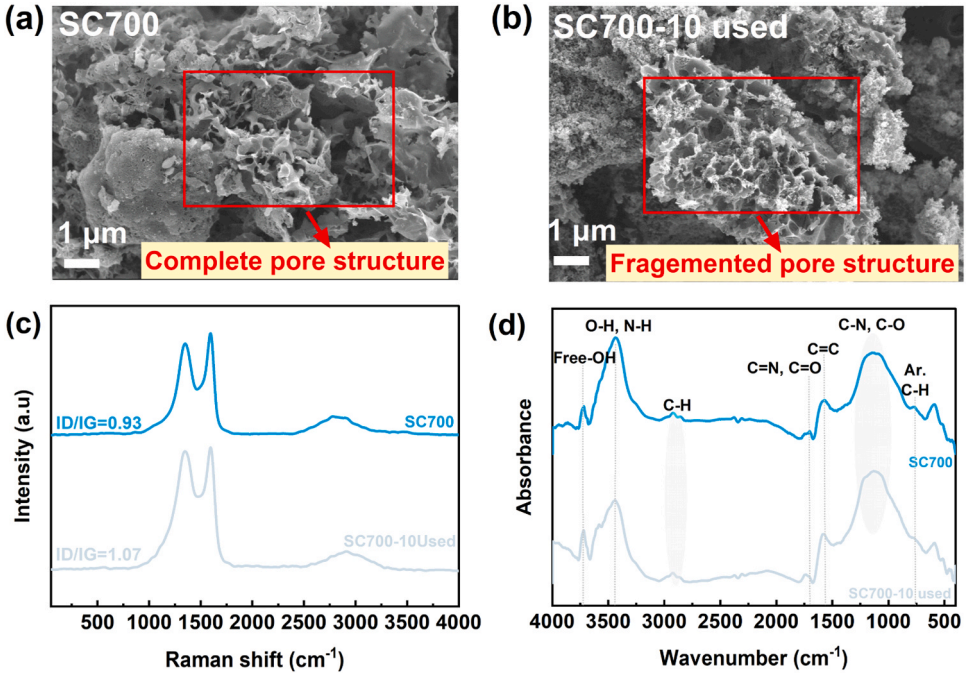

Fig. 13. SEM images of (a) SC700 and (b) SC700–10 used, (c) Raman spectra and (d) FTIR spectra for SC700 and SC700–10 used.

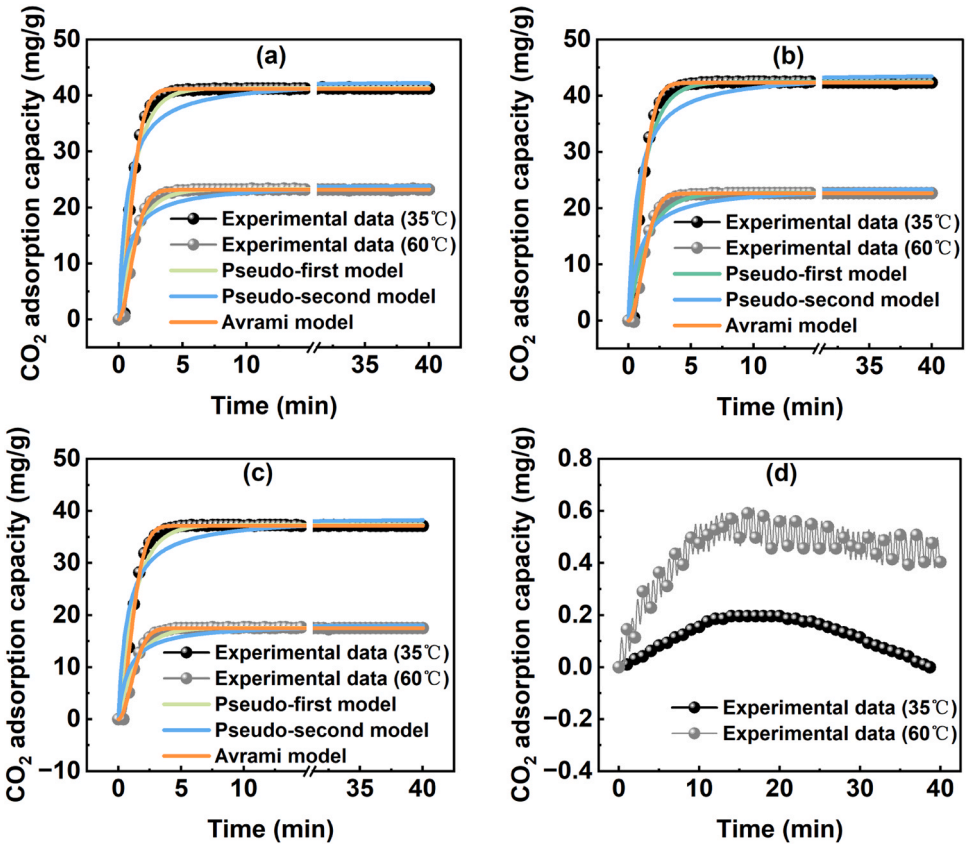

Fig. 14. Kinetics of CO_2 adsorption on (a) SC600, (b)SC700, (c) SC800 and (d) S700 at 35 and 60 °C.

Table 8
Adsorption kinetics parameters of CO_2 adsorption at 35 and 60 °C for biochars.

Model	Pseudo-first-order model			Pseudo-second-order model			Avrami model			
Equations	$q_t = q_e(1 - e^{-k_1 t})$			$q_t = \frac{t \cdot k_2 \cdot q_e^2}{1 + q_e \cdot t \cdot k_2}$			$q_t = q_e(1 - e^{-(k_3 t)^n})$			
Parameters	$q_{e,cal}$ mg/g	k_1 min^{-1}	R^2	$q_{e,cal}$ mg/g	k_2 g/(mg·min)$^{-1}$	R^2	$q_{e,cal}$ mg/g	k_3 min^{-1}	n	R^2
SC600–35	41.34	0.83	0.963	42.96	0.04	0.864	41.19	0.80	1.59	0.990
SC600–60	23.29	0.74	0.958	23.29	0.06	0.856	23.18	0.72	1.71	0.993
SC700–35	42.50	0.78	0.962	44.23	0.03	0.858	42.33	0.75	1.63	0.992
SC700–60	22.76	0.66	0.950	23.86	0.05	0.848	22.64	0.64	1.86	0.994
SC800–35	37.35	0.74	0.956	38.95	0.04	0.850	37.19	0.72	1.74	0.994
SC800–60	17.56	0.69	0.948	18.36	0.07	0.839	17.48	0.67	1.85	0.994

performance of SCs and S700, a linear analysis was performed between S_M, V_M, S_{UM}, V_{UM}, N content, O/C ratio and CO_2 adsorption capacity, as illustrated in Fig. 15. Regardless of the adsorption temperatures, the R^2 values for S_{UM} (0.550–0.821) and V_{UM} (0.775–0.962) were considerably higher than those for S_M (0.109–0.352), V_M (0.094–0.328), N content (0.205–0.483) and O/C ratio (0.284–0.575). This indicates that CO_2 adsorption onto biochar primarily occurs through physical adsorption, with the pore volume and pore area of ultra-micropores playing a more significant role than other factors.

3.4.3. IAST Selectivity analysis

In the context of post-combustion carbon capture technology, the CO_2/N_2 selectivity of the adsorbent is extremely important. This study utilized the Ideal Adsorbed Solution Theory (IAST) to determine selectivity by analyzing the single-component adsorption isotherms of CO_2 and N_2. The detailed calculation equation can be found in the selectivity section of the Supplementary Material. As shown in Fig. 16, the CO_2/N_2 selectivity decreased with an increasing volume fraction of CO_2 across all biochar samples. The order of CO_2/N_2 selectivity was as follows: SC600 > SC700 > SC800 > S700. Notably, the selectivity of SC600 and SC700 at a composition of 10 % CO_2 and 90 % N_2 remained relatively high of greater than 60. Additionally, the selectivity of SCs was significantly higher than that of S700, particularly under conditions of low CO_2 partial pressure. This implies that the co-pyrolysis of TDS and corncob can enhance the CO_2/N_2 selectivity of biochar.

3.4.4. Isosteric adsorption heat and adsorption-desorption cycles

The isosteric adsorption heat (Q_{st}) is a crucial parameter for characterizing the surface energy heterogeneity of an adsorbent. A lower Q_{st} value indicates that the adsorbate can be more easily desorbed. As illustrated in Fig. 17 (a), Q_{st} was calculated using the Clausius-Clapeyron equation based on the CO_2 adsorption isotherms of the SCs at 25 and 50 °C. The detailed calculation equation can be found in the isosteric adsorption heat section of the Supplementary Material. The Q_{st} values for the SCs ranged from 20 to 24 kJ/mol, suggesting that the energy required for the regeneration was relatively low. Additionally, Q_{st}

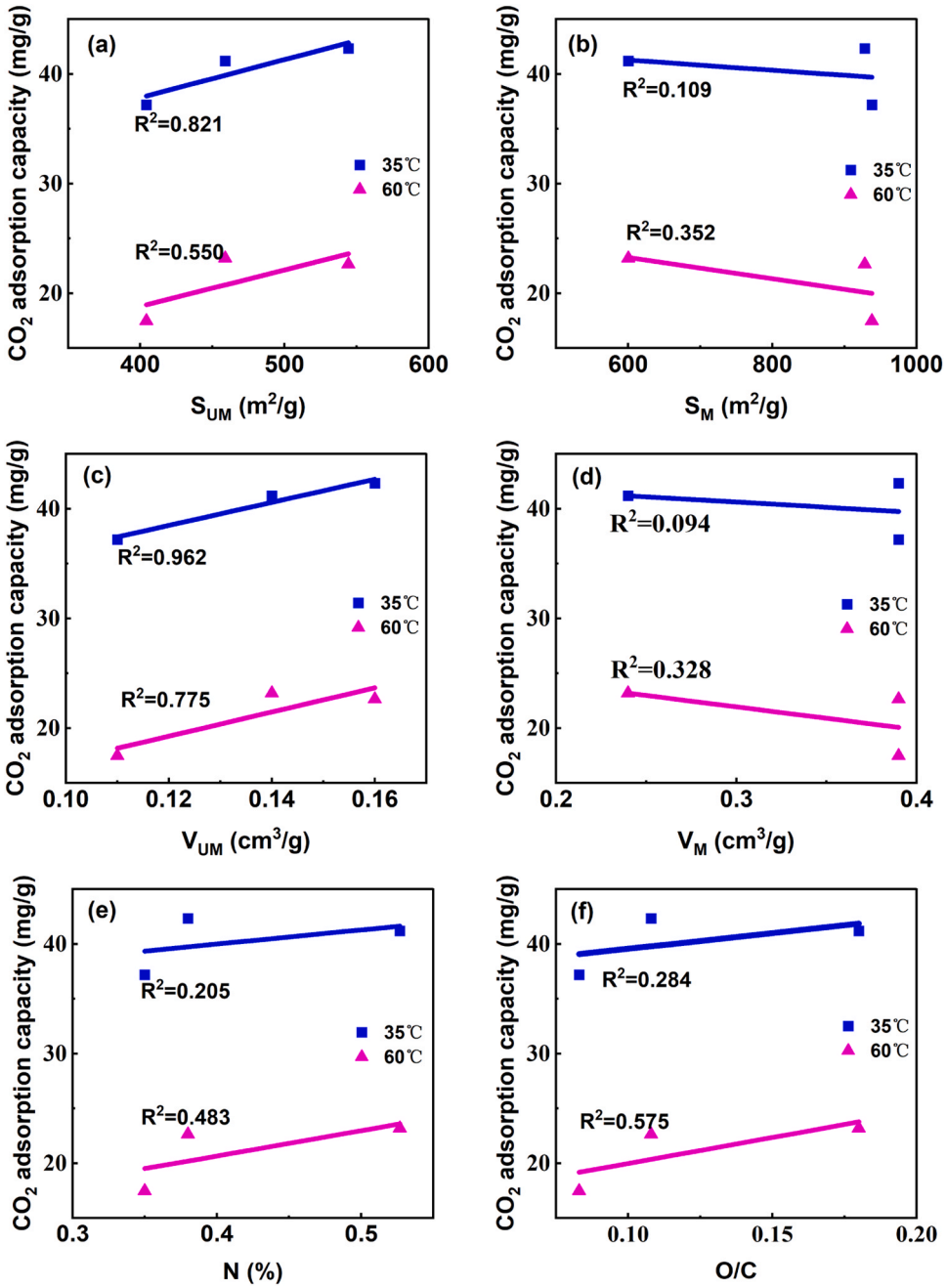

Fig. 15. Relationships between basic physiochemical properties and CO_2 dynamic adsorption capacity: (a) S_{UM}, (b) S_M, (c) V_{UM}, (d) V_M, (e) N content, and (f) O/C ratio.

decreased as the amount of adsorbed CO_2 increased. This trend occurred because the CO_2 adsorption sites became progressively occupied, leading to an increase in the repulsive interaction energy among CO_2 molecules and a decrease in the attractive interaction energy between CO_2 and biochar. Notably, SC700 exhibited the highest Q_{st}, indicating a stronger interaction between SC700 and CO_2. Fig. 17 (b) presents the ten-cycle adsorption capacities of SC700 at a regeneration temperature of 100 °C. Initially, the CO_2 adsorption capacity was 114.2 mg/g. After ten cycles, it remained above 110 mg/g, with a relative change in CO_2 adsorption capacity between the first and tenth cycles of no more than 1.5 %. This indicates that SC700 possessed a relatively high and stable cyclic adsorption capability.

3.5. Cost of producing SC700

The economic analysis of industrial-scale production was estimated using the method reported by Mukherjee et al.[72] and Serafin et al. [73]. According to the results of co-pyrolysis experiments, the production yield of SC700 was 10 %. We assumed that 10 tons of dry TDS and 10 tons of dry corncobs were co-pyrolyzed daily, resulting in a final output of 2 tons of SC700 each day. Detailed calculation information is provided in cost of producing SC700 section in the supplementary materials.

According to the Table 9 and Table 10, the estimated cost of producing SC700 from TDS and corncobs was 1.37 €/kg. This cost was lower than that of other biochars, further demonstrating that recycling TDS and corncob into valuable biochars is an environmentally friendly and cost-effective method for effectively capturing CO_2.

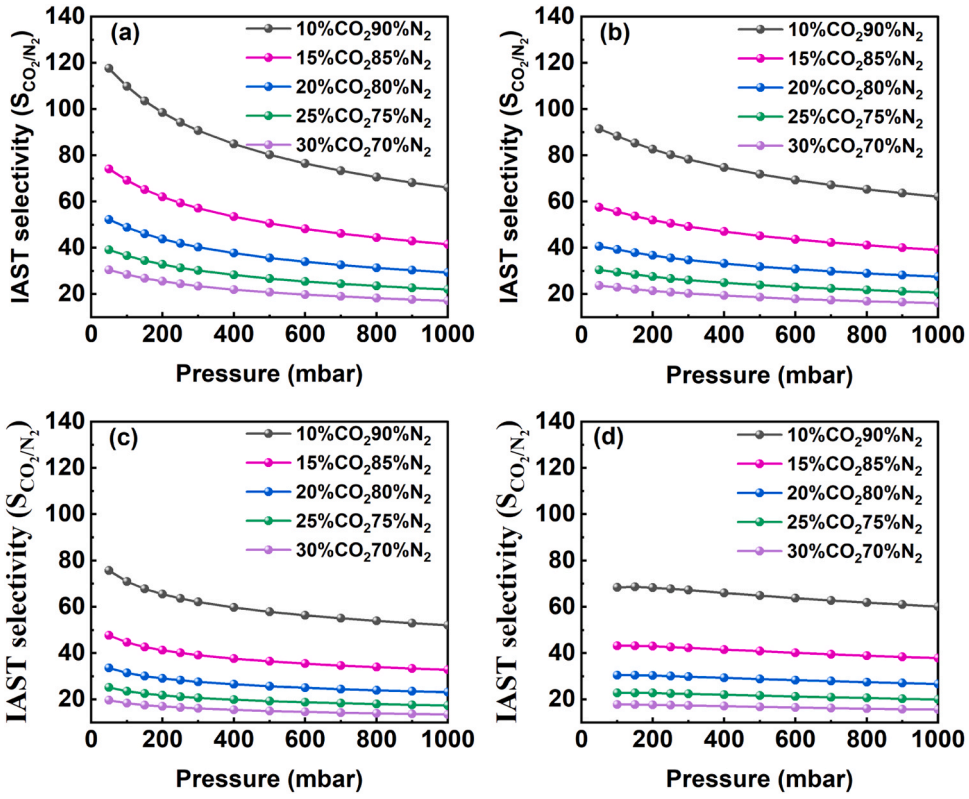

Fig. 16. IAST selectivity of (a) SC600, (b) SC700, (c) SC800 and (d) S700 under different ratios of CO_2/N_2 at 25 °C.

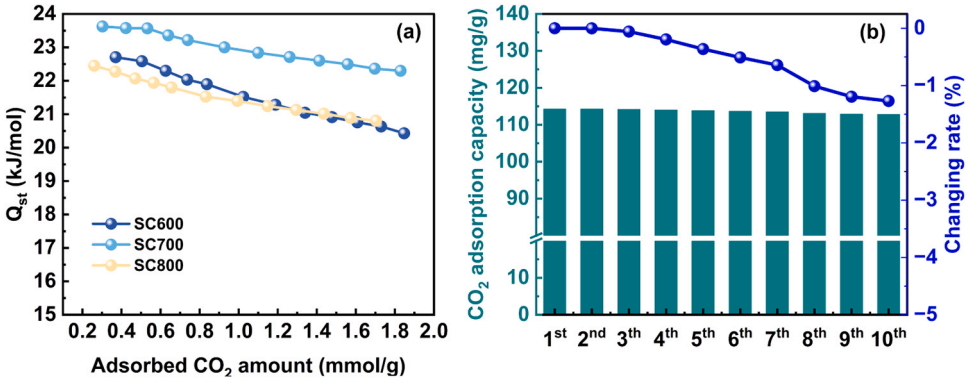

Fig. 17. (a) Q_{st} of SCs and (b) cyclic adsorption capacity and relative change of SC700.

Table 9
Summary of costs.

Total capital investment (C_{TCI})	16354578 €
Total operational costs (C_{TOC})	823181 €
Depreciation (C_D)	51789 €
Estimated annual production of biochar	640 t
Estimated cost for biochar	1.37 €/kg

Table 10
Production costs of SC700 and other biochars.

Raw material	Cost	Reference
Face mask waste	2.10 €/kg	[73]
Tires	9.81 €/kg	[74]
Wood	5.49 €/kg	[74]
Lignite	4.62 €/kg	[74]
TDS and corncob	1.37 €/kg	This study

3.6. *The feasibility of application under real industrial conditions*

The comparison of CO_2 adsorption performance among various biochars section in the supplementary material offers a more comprehensive and globally representative analysis. Among the biochars, SC700 exhibited a relatively high capacity for CO_2 adsorption, along with notable CO_2/N_2 selectivity and cyclic stability compared to other biochars. Although the CO_2 adsorption capacity we obtained was not the highest, SC700 still remained competitive. Furthermore, the manufacturing cost of SC700 was lower than that of the activated carbon reported in the literature[73,74]. These advantages indicate that SC700 holds significant potential for practical industrial applications.

4. Conclusion

In this study, the co-pyrolysis interaction between TDS and corncob was analyzed. The reaction between alkali and alkaline earth metals and the organic substances in corncob and TDS leads to synergistic and self-catalytic effects. These effects can enhance biochar yield and optimize the ultra-micropore structure that is crucial for CO_2 adsorption. The obtained biochar was characterized in N_2 sorption investigations, as well as SEM, XRD, Raman analysis and FTIR spectroscopy.

In terms of texture features, SC700 distinguished itself among the SCs due to its the highest specific surface area of ultra-micropores (544.38 m^2/g) and ultra-micropore volume (0.16 cm^3/g). Notably, SC700 achieved the most significant CO_2 adsorption capacity at 25 °C (128.1 mg/g) among the SCs, which was more than double that of the TDS biochar. It was found that the adsorption mechanisms for the SCs and S700 were predominantly governed by physical adsorption. Furthermore, SC700 exhibited the best thermal stability among the SCs, with a remarkably low carbon skeleton mass loss of only 6.71 %. The thermal oxidation stability of the SCs also improved as the activation temperature increased. Additionally, SC700 exhibited excellent cyclic performance in ten cycles of CO_2 adsorption and desorption experiments, showing a minimal decrease of no more than 1.5 %. Notably, SC700 had a high pyridine nitrogen content (40.58 %), which provided abundant sites for CO_2 chemisorption. This finding is consistent with the results of the *in situ* DRIFT spectra and contributes to the highest Q_{st} among the SCs. The comparisons between SC700 and various biochar worldwide, along with the economic analysis results, further suggest the potential of biochar produced from TDS and corncob as effective adsorbents for CO_2 separation.

This study provides a theoretical foundation and practical insights for developing novel biochar for CO_2 capture, contributing to the exploration of more effective CO_2 absorbents to combat global warming.

CRediT authorship contribution statement

Wang Jun: Resources, Investigation. **Huang Qunxing:** Writing – review & editing, Supervision, Funding acquisition, Conceptualization. **Pan Yu:** Writing – original draft, Methodology, Formal analysis, Data curation, Conceptualization. **Lei Jiahui:** Writing – review & editing, Resources, Data curation. **Song Kun:** Resources, Investigation. **Huang Lanfang:** Resources, Investigation. **Zhang Zehuang:** Writing – review & editing, Investigation. **Lou Fangfang:** Writing – review & editing, Resources.

Declaration of Competing Interest

The authors declare that they have no known competing financial interests or personal relationships that could have appeared to influence the work reported in this paper.

Acknowledgments

The authors would like to gratefully acknowledge Basic Public Welfare Research Program of Zhejiang Province (LBMHY24E060002).

Appendix A. Supporting information

Supplementary data associated with this article can be found in the online version at doi:10.1016/j.jcou.2025.103079.

Data Availability

Data will be made available on request.

References

[1] W.-H. Xie, H. Li, M. Yang, L.-N. He, H.-R. Li, CO_2 capture and utilization with solid waste, Green. Chem. Eng. 3 (3) (2022) 199–209, https://doi.org/10.1016/j.gce.2022.01.002.
[2] W. Tang, L. Luo, Y. Chen, J. Li, Y. Dai, Y. Xie, Y. Ma, J. Zhang, Y. Zhang, Noble-metal-free bi-ozis nanohybrids for sacrificial-agent-free photocatalytic water splitting: with long-lived photogenerated electrons, Sep. Purif. Technol. 357 (2025) 130047, https://doi.org/10.1016/j.seppur.2024.130047.
[3] L. Luo, L. Zhang, H. Ye, Y. Dai, Y. Xie, Y. Chen, Z. Wang, Y. Zhang, Synchronous promotion of znin2s4 sacrificial agent-free photocatalytic hydrogen production by non-metallic doping and construction of heterojunction, Sep. Purif. Technol. 360 (2025) 131102, https://doi.org/10.1016/j.seppur.2024.131102.
[4] A. Zaker, S. ben Hammouda, J. Sun, X. Wang, X. Li, Z. Chen, Carbon-based materials for CO_2 capture: their production, modification and performance, J. Environ. Chem. Eng. 11 (3) (2023) 109741, https://doi.org/10.1016/j.jece.2023.109741.
[5] K. Li, D. Zhang, X. Niu, H. Guo, Y. Yu, Z. Tang, Z. Lin, M. Fu, Insights into CO_2 Adsorption on KOH-activated biochars derived from the mixed sewage sludge and pine sawdust, Sci. Total Environ. 826 (2022) 154133, https://doi.org/10.1016/j.scitotenv.2022.154133.
[6] Y. Zhang, M. He, L. Wang, J. Yan, B. Ma, X. Zhu, Y.S. Ok, V. Mechtcherine, D.C. W. Tsang, Biochar as construction materials for achieving carbon neutrality, Biochar 4 (1) (2022) 59, https://doi.org/10.1007/s42773-022-00182-x.
[7] Z. Ghanbarpour Mamaghani, K.A. Hawboldt, S. MacQuarrie, Adsorption of CO_2 Using biochar - review of the impact of gas mixtures and water on adsorption, J. Environ. Chem. Eng. 11 (3) (2023) 109643, https://doi.org/10.1016/j.jece.2023.109643.
[8] H. Liu, Y. Wang, S. Zhao, H. Hu, C. Cao, A. Li, Y. Yu, H. Yao, Review on the current status of the co-combustion technology of organic solid waste (OSW) and Coal in China, Energy Fuels 34 (12) (2020) 15448–15487, https://doi.org/10.1021/acs.energyfuels.0c02177.
[9] L. Zhao, Z.-F. Sun, X.-W. Pan, J.-Y. Tan, S.-S. Yang, J.-T. Wu, C. Chen, Y. Yuan, N.-Q. Ren, Sewage sludge derived biochar for environmental improvement: advances, challenges, and solutions, Water Res. X 18 (2023) 100167, https://doi.org/10.1016/j.wroa.2023.100167.
[10] M.M. Mian, W. Ao, S. Deng, Sludge-based biochar adsorbent: pore tuning mechanisms, challenges, and role in carbon sequestration, Biochar 5 (1) (2023) 83, https://doi.org/10.1007/s42773-023-00288-w.
[11] H. Zhang, Z. Gao, W. Ao, J. Li, G. Liu, J. Fu, C. Ran, X. Mao, Q. Kang, Y. Liu, J. Dai, Microwave pyrolysis of textile dyeing sludge in a continuously operated auger reactor: char characterization and analysis, J. Hazard. Mater. 334 (2017) 112–120, https://doi.org/10.1016/j.jhazmat.2017.03.048.
[12] Y. Song, J. Hu, J. Liu, F. Evrendilek, M. Buyukada, CO_2-assisted co-pyrolysis of textile dyeing sludge and hyperaccumulator biomass: dynamic and comparative analyses of evolved gases, bio-oils, biochars, and reaction mechanisms, J. Hazard. Mater. 400 (2020) 123190, https://doi.org/10.1016/j.jhazmat.2020.123190.
[13] M.M. Mian, G. Liu, Activation of peroxymonosulfate by chemically modified sludge biochar for the removal of organic pollutants: understanding the role of active sites and mechanism, Chem. Eng. J. 392 (2020) 123681, https://doi.org/10.1016/j.cej.2019.123681.
[14] Y. Liu, C. Ran, A.A. Siyal, Y. Song, Z. Jiang, J. Dai, P. Chtaeva, J. Fu, W. Ao, Z. Deng, T. Zhang, Comparative study for fluidized bed pyrolysis of textile dyeing sludge and municipal sewage sludge, J. Hazard. Mater. 396 (2020) 122619, https://doi.org/10.1016/j.jhazmat.2020.122619.
[15] A. Yadav, P. Yadav, S. Bojjagani, J.K. Srivastava, A. Raj, Investigation of the speciation and environmental risk of heavy metals in biochar produced from textile sludge waste by pyrolysis at different temperatures, Chemosphere 360 (2024) 142454, https://doi.org/10.1016/j.chemosphere.2024.142454.
[16] X. Xu, Y. Kan, L. Zhao, X. Cao, Chemical Transformation of CO_2 during its capture by waste biomass derived biochars, Environ. Pollut. 213 (2016) 533–540, https://doi.org/10.1016/j.envpol.2016.03.013.
[17] R. Khan, S. Shukla, M. Kumar, A. Zuorro, A. Pandey, Sewage sludge derived biochar and its potential for sustainable environment in circular economy: advantages and challenges, Chem. Eng. J. 471 (2023) 144495, https://doi.org/10.1016/j.cej.2023.144495.
[18] Q. Dai, W. Xiang, Q. Liu, M. Wang, X. Zhang, Co-pyrolysis biochar derived from sewage sludge and lignin: synergetic effect and adsorption properties, J. Environ. Chem. Eng. 10 (3) (2022) 107898, https://doi.org/10.1016/j.jece.2022.107898.
[19] Z. Zhang, Q. Guo, L. Jiao, X. Wang, M. Li, N. Zhou, Y. Hu, Insights into the microstructure evolution and CO_2 adsorption of activated carbon derived from spent coffee grounds and sewage sludge, Biomass-.-. Convers. Biorefinery 14 (23) (2024) 29775–29786, https://doi.org/10.1007/s13399-023-04878-3.
[20] W. Wu, J. Liu, G. Zhang, Y. Wang, C. Wu, G. Li, Y. Zhao, Adsorption of CO_2 by sludge/bamboo shoot shell hybrid biochar prepared by a single-step K_2CO_3 activation, Fuel 381 (2025) 133555, https://doi.org/10.1016/j.fuel.2024.133555.
[21] Q. Dai, Q. Liu, X. Zhang, L. Cao, B. Hu, J. Shao, F. Ding, X. Guo, B. Gao, Synergetic effect of co-pyrolysis of sewage sludge and lignin on biochar production and adsorption of methylene blue, Fuel 324 (2022) 124587, https://doi.org/10.1016/j.fuel.2022.124587.
[22] B. Li, W. Wei, Effect of lignin on the co-pyrolysis of sludge and cellulose, Energy Sources Part Recovery Util. Environ. Eff. 38 (12) (2016) 1825–1831, https://doi.org/10.1080/15567036.2014.964816.
[23] K. Li, X. Niu, D. Zhang, H. Guo, X. Zhu, H. Yin, Z. Lin, M. Fu, Renewable biochar derived from mixed sewage sludge and pine sawdust for carbon dioxide capture,

Environ. Pollut. 306 (2022) 119399, https://doi.org/10.1016/j.envpol.2022.119399.
[24] Y. Xiao, A. Raheem, L. Ding, W.-H. Chen, X. Chen, F. Wang, S.-L. Lin, Pretreatment, modification and applications of sewage sludge-derived biochar for resource recovery- a review, Chemosphere 287 (2022) 131969, https://doi.org/10.1016/j.chemosphere.2021.131969.
[25] Z. Wang, Q. Tian, J. Guo, R. Wu, H. Zhu, H. Zhang, Co-pyrolysis of sewage sludge/cotton stalks with K2CO3 for biochar production: improved biochar porosity and reduced heavy metal leaching, Waste Manag 135 (2021) 199–207, https://doi.org/10.1016/j.wasman.2021.08.042.
[26] J. Zhu, J. Yang, Y. Fan, H. Zhang, H. Fan, X. Zhang, H. Yang, H. Chen, S. Zhang, Research on the interaction mechanism between textile dyeing sludge and biomass components during high-temperature co-pyrolysis, Fuel 372 (2024) 132156, https://doi.org/10.1016/j.fuel.2024.132156.
[27] J. Huang, J. Liu, K. Chang, M. Buyukada, F. Evrendilek, Co-)Pyrolytic performances and by-products of textile dyeing sludge and spent mushroom substrate, J. Clean. Prod. 261 (2020) 121195, https://doi.org/10.1016/j.jclepro.2020.121195.
[28] Y. Li, T. Zhang, Y. Wang, B. Wang, Transformation of waste cornstalk into versatile porous carbon adsorbent for selective CO_2 Capture and Efficient Methanol Adsorption, J. Environ. Chem. Eng. 9 (5) (2021) 106149, https://doi.org/10.1016/j.jece.2021.106149.
[29] Z. Xu, M. He, X. Xu, X. Cao, D.C.W. Tsang, Impacts of different activation processes on the carbon stability of biochar for oxidation resistance, Bioresour. Technol. 338 (2021) 125555, https://doi.org/10.1016/j.biortech.2021.125555.
[30] O.R. Harvey, L.-J. Kuo, A.R. Zimmerman, P. Louchouarn, J.E. Amonette, B. E. Herbert, An index-based approach to assessing recalcitrance and soil carbon sequestration potential of engineered black carbons (Biochars), Environ. Sci. Technol. 46 (3) (2012) 1415–1421, https://doi.org/10.1021/es2040398.
[31] J. Zhang, H. Zou, J. Liu, F. Evrendilek, W. Xie, Y. He, M. Buyukada, Comparative (co-)pyrolytic performances and by-products of textile dyeing sludge and cattle manure: deeper insights from Py-GC/MS, TG-FTIR, 2D-COS and PCA analyses, J. Hazard. Mater. 401 (2021) 123276, https://doi.org/10.1016/j.jhazmat.2020.123276.
[32] X. Wang, S. Deng, H. Tan, A. Adeosun, M. Vujanović, F. Yang, N. Duić, Synergetic effect of sewage sludge and biomass co-pyrolysis: a combined study in thermogravimetric analyzer and a fixed bed reactor, Energy Convers. Manag 118 (2016) 399–405, https://doi.org/10.1016/j.enconman.2016.04.014.
[33] W. Wang, R. Lemaire, A. Bensakhria, D. Luart, Review on the catalytic effects of alkali and alkaline earth metals (aaems) including sodium, potassium, calcium and magnesium on the pyrolysis of lignocellulosic biomass and on the co-pyrolysis of coal with biomass, J. Anal. Appl. Pyrolysis 163 (2022) 105479, https://doi.org/10.1016/j.jaap.2022.105479.
[34] X. Peng, X. Ma, Y. Lin, Z. Guo, S. Hu, X. Ning, Y. Cao, Y. Zhang, Co-pyrolysis between microalgae and textile dyeing sludge by TG–FTIR: kinetics and products, Energy Convers. Manag 100 (2015) 391–402, https://doi.org/10.1016/j.enconman.2015.05.025.
[35] S. Deng, X. Wang, H. Tan, H. Mikulčić, F. Yang, Z. Li, N. Duić, Thermogravimetric study on the co-combustion characteristics of oily sludge with plant biomass, Thermochim. Acta 633 (2016) 69–76, https://doi.org/10.1016/j.tca.2016.03.006.
[36] X. Xiao, B. Chen, Z. Chen, L. Zhu, J.L. Schnoor, Insight into multiple and multilevel structures of biochars and their potential environmental applications: a critical review, Environ. Sci. Technol. 52 (9) (2018) 5027–5047, https://doi.org/10.1021/acs.est.7b06487.
[37] E. Pusceddu, S.F. Santilli, G. Fioravanti, A. Montanaro, F. Miglietta, P.U. Foscolo, Chemical-physical analysis and exfoliation of biochar-carbon matter: from agriculture soil improver to starting material for advanced nanotechnologies, Mater. Res. Express 6 (11) (2019) 115612, https://doi.org/10.1088/2053-1591/ab4ba8.
[38] G. Chen, H. Yu, F. Lin, Z. Zhang, B. Yan, Y. Song, Utilization of edible fungi residues towards synthesis of high-performance porous carbon for effective sorption of Cl-VOCs, Sci. Total Environ. 727 (2020) 138475, https://doi.org/10.1016/j.scitotenv.2020.138475.
[39] B. Dziejarski, R. Faust, J. Serafin, R. Krzyżyńska, K. Andersson, P. Knutsson, Insights into activation pathways of recovered carbon black (rCB) from end-of-life tires (elts) by potassium-containing agents, ACS Omega 9 (29) (2024) 31814–31831, https://doi.org/10.1021/acsomega.4c03160.
[40] T. Guo, Y. Zhang, Y. Geng, J. Chen, Z. Zhu, A.H. Bedane, Y. Du, Surface oxidation modification of nitrogen doping biochar for enhancing CO_2 adsorption, Ind. Crops Prod. 206 (2023) 117582, https://doi.org/10.1016/j.indcrop.2023.117582.
[41] S. Gu, J. He, Y. Zhu, Z. Wang, D. Chen, G. Yu, C. Pan, J. Guan, K. Tao, Facile carbonization of microporous organic polymers into hierarchically porous carbons targeted for effective CO_2 uptake at low pressures, ACS Appl. Mater. Interfaces 8 (28) (2016) 18383–18392, https://doi.org/10.1021/acsami.6b05170.
[42] H. Li, M. Tang, X. Huang, L. Wang, Q. Liu, S. Lu, An Efficient Biochar Adsorbent for CO_2 capture: combined experimental and theoretical study on the promotion mechanism of *N*-Doping, Chem. Eng. J. 466 (2023) 143095, https://doi.org/10.1016/j.cej.2023.143095.
[43] A. Oya, N. Kishimoto, S. Mashio, K. Kumakura, T. Suzuki, B. Serrano-Talavera, A. Linares-Solano, Structure and properties of a moulded carbon derived from rice Hull, J. Mater. Sci. 30 (24) (1995) 6249–6252, https://doi.org/10.1007/BF00369673.
[44] Y. Li, B. Zou, C. Hu, M. Cao, Nitrogen-doped porous carbon nanofiber webs for efficient CO_2 capture and conversion, Carbon 99 (2016) 79–89, https://doi.org/10.1016/j.carbon.2015.11.074.
[45] H. Wang, X. Li, Z. Cui, Z. Fu, L. Yang, G. Liu, M. Li, Coffee grounds derived N enriched microporous activated carbons: efficient adsorbent for post-combustion CO_2 capture and conversion, J. Colloid Interface Sci. 578 (2020) 491–499, https://doi.org/10.1016/j.jcis.2020.05.125.
[46] A.N. Shafawi, P. Lahijani, M. Mohammadi, A.R. Mohamed, An Investigation on sequential ultrasonication and metal modification of biochar on Its CO_2 capture performance, Biomass-.-. Convers. Biorefinery 14 (22) (2024) 28571–28587, https://doi.org/10.1007/s13399-022-03658-9.
[47] W. Jia, H. Wang, Q. Wu, L. Sun, Q. Si, Q. Zhao, Y. Wu, N. Ren, W. Guo, Insight into chinese medicine residue biochar combined with ultrasound for persulfate activation in atrazine degradation: *Acanthopanax Senticosus* precursors, synergistic effects and toxicity assessment, Sci. Total Environ. 880 (2023) 163054, https://doi.org/10.1016/j.scitotenv.2023.163054.
[48] N. Liu, X. Song, C. Wang, K. Li, P. Ning, X. Sun, F. Wang, Y. Ma, Surface characterization study of corn-straw biochar catalysts for the simultaneous removal of HCN, COS, and CS_2, N. J. Chem. 44 (32) (2020) 13565–13575, https://doi.org/10.1039/D0NJ01648A.
[49] C.H. Chia, B. Gong, S.D. Joseph, C.E. Marjo, P. Munroe, A.M. Rich, Imaging of Mineral-Enriched Biochar by FTIR, Raman and SEM–EDX, Vib. Spectrosc. 62 (2012) 248–257, https://doi.org/10.1016/j.vibspec.2012.06.006.
[50] J. Xu, Y. Zhang, B. Li, S. Fan, H. Xu, D.-X. Guan, Improved adsorption properties of tetracycline on KOH/$KMnO_4$ modified biochar derived from wheat straw, Chemosphere 296 (2022) 133981, https://doi.org/10.1016/j.chemosphere.2022.133981.
[51] X. Zhang, S. Zhang, H. Yang, Y. Feng, Y. Chen, X. Wang, H. Chen, Nitrogen enriched biochar modified by high temperature CO_2–ammonia treatment: characterization and adsorption of CO_2, Chem. Eng. J. 257 (2014) 20–27, https://doi.org/10.1016/j.cej.2014.07.024.
[52] J. Serafin, B. Dziejarski, Ó.J. Fonseca-Bermúdez, L. Giraldo, R. Sierra-Ramírez, M. G. Bonillo, G. Farid, J.C. Moreno-Piraján, Bioorganic activated carbon from cashew nut shells for H_2 Adsorption and H_2/CO_2, H_2/CH_4, CO_2/CH_4, $H_2/CO_2/CH_4$ selectivity in industrial applications, Int. J. Hydrog. Energy 86 (2024) 662–676, https://doi.org/10.1016/j.ijhydene.2024.08.417.
[53] J. Shao, J. Zhang, X. Zhang, Y. Feng, H. Zhang, S. Zhang, H. Chen, Enhance SO_2 adsorption performance of biochar modified by CO_2 activation and amine impregnation, Fuel 224 (2018) 138–146, https://doi.org/10.1016/j.fuel.2018.03.064.
[54] B. Li, D. Liu, D. Lin, X. Xie, S. Wang, H. Xu, J. Wang, Y. Huang, S. Zhang, X. Hu, Changes in biochar functional groups and its reactivity after volatile–char interactions during biomass pyrolysis, Energy Fuels 34 (11) (2020) 14291–14299, https://doi.org/10.1021/acs.energyfuels.0c03243.
[55] J. Chen, P. Wang, L. Ding, T. Yu, S. Leng, J. Chen, L. Fan, J. Li, L. Wei, J. Li, Q. Lu, L. Leng, W. Zhou, The comparison study of multiple biochar stability assessment methods, J. Anal. Appl. Pyrolysis 156 (2021) 105070, https://doi.org/10.1016/j.jaap.2021.105070.
[56] S. Lu, X. Huang, M. Tang, Y. Peng, S. Wang, C.P. Makwarimba, Synthesis of n-doped hierarchical porous carbon with excellent toluene adsorption properties and its activation mechanism, Environ. Pollut. 284 (2021) 117113, https://doi.org/10.1016/j.envpol.2021.117113.
[57] A. Pourjavadi, H. Abdolmaleki, M. Doroudian, S.H. Hosseini, Novel synthesis route for preparation of porous nitrogen-doped carbons from lignocellulosic wastes for high performance supercapacitors, J. Alloy. Compd. 827 (2020) 154116, https://doi.org/10.1016/j.jallcom.2020.154116.
[58] J. Chen, J. Lin, J. Luo, Z. Tian, J. Zhang, S. Sun, Y. Shen, R. Ma, Enhanced CO_2 Capture Performance of N, S Co-doped biochar prepared by microwave pyrolysis: synergistic modulation of microporous structure and functional groups, Fuel 379 (2025) 132987, https://doi.org/10.1016/j.fuel.2024.132987.
[59] L. Spessato, V.A. Duarte, J.M. Fonseca, P.A. Arroyo, V.C. Almeida, Nitrogen-doped activated carbons with high performances for CO_2 adsorption, J. CO2 Util. 61 (2022) 102013, https://doi.org/10.1016/j.jcou.2022.102013.
[60] L. Leng, H. Huang, H. Li, J. Li, W. Zhou, Biochar stability assessment methods: a review, Sci. Total Environ. 647 (2019) 210–222, https://doi.org/10.1016/j.scitotenv.2018.07.402.
[61] B. Liu, X. Ma, R. Shi, K. Zhou, X. Xu, J. Qiu, H. Wang, Z. Zeng, L. Li, Synthesis of alkali metals functionalized porous carbon for enhanced selective adsorption of carbon dioxide: a theoretically guided study, Energy Fuels 35 (19) (2021) 15962–15968, https://doi.org/10.1021/acs.energyfuels.1c02313.
[62] L. Cao, X. Zhang, Y. Xu, W. Xiang, R. Wang, F. Ding, P. Hong, B. Gao, Straw and wood based biochar for CO_2 capture: adsorption performance and governing mechanisms, Sep. Purif. Technol. 287 (2022) 120592, https://doi.org/10.1016/j.seppur.2022.120592.
[63] J. Serafin, B. Dziejarski, Application of isotherms models and error functions in activated carbon co2 sorption processes, Microporous Mesoporous Mater. 354 (2023) 112513, https://doi.org/10.1016/j.micromeso.2023.112513.
[64] Y. Li, G. Zhang, C. Wu, J. Liu, G. Li, Y. Wang, Y. Zhao, Novel nitrogen-enriched activated carbon with tunable microporosity from agricultural and plastic waste for CO_2 adsorption, J. Environ. Chem. Eng. 11 (6) (2023) 111257, https://doi.org/10.1016/j.jece.2023.111257.
[65] Gautam, J. Serafin, S. Vikram, B. Dziejarski, S. Sahoo, An environmentally friendly synthesis method of activated carbons based on subabul (*Leucaena leucocephala*) sawdust waste for CO_2 adsorption, J. Clean. Prod. 412 (2023) 137406, https://doi.org/10.1016/j.jclepro.2023.137406.
[66] P. Ammendola, F. Raganati, R. Chirone, CO_2 adsorption on a fine activated carbon in a sound assisted fluidized bed: thermodynamics and kinetics, Chem. Eng. J. 322 (2017) 302–313, https://doi.org/10.1016/j.cej.2017.04.037.

[67] K. Li, D. Zhang, X. Niu, M. Liu, Z. Tang, Yongming Zhong, X. Yu, Y. Zhu, CO_2 Adsorption mechanisms on activated nano-sized biocarbons: investigation through *in Situ* DRIFTS, quasi in-situ XPS and XRD, Sep. Purif. Technol. 315 (2023) 123538, https://doi.org/10.1016/j.seppur.2023.123538.

[68] J. Dong, R. Wang, X. Wang, S. Tan, Z. Zhao, Q. Yin, X. Lu, Preparation of lignin-based porous carbon through thermochemical activation and nitrogen doping for co2 selective adsorption, Carbon 229 (2024) 119530, https://doi.org/10.1016/j.carbon.2024.119530.

[69] Y. Hosakun, K. Halász, M. Horváth, L. Csóka, V. Djoković, ATR-FTIR study of the interaction of CO_2 with bacterial cellulose-based membranes, Chem. Eng. J. 324 (2017) 83–92, https://doi.org/10.1016/j.cej.2017.05.029.

[70] H. Gong, Z. Tan, L. Zhang, Q. Huang, Preparation of biochar with high absorbability and its nutrient adsorption–desorption behaviour, Sci. Total Environ. 694 (2019) 133728, https://doi.org/10.1016/j.scitotenv.2019.133728.

[71] G. Singh, I.Y. Kim, K.S. Lakhi, P. Srivastava, R. Naidu, A. Vinu, Single step synthesis of activated bio-carbons with a high surface area and their excellent CO_2 adsorption capacity, Carbon 116 (2017) 448–455, https://doi.org/10.1016/j.carbon.2017.02.015.

[72] A. Mukherjee, J.A. Okolie, C. Niu, A.K. Dalai, Techno – economic analysis of activated carbon production from spent coffee grounds: comparative evaluation of different production routes, Energy Convers. Manag. X 14 (2022) 100218, https://doi.org/10.1016/j.ecmx.2022.100218.

[73] J. Serafin, J. Sreńscek-Nazzal, A. Kamińska, O. Paszkiewicz, B. Michalkiewicz, Management of surgical mask waste to activated carbons for CO_2 Capture, J. CO2 Util. 59 (2022) 101970, https://doi.org/10.1016/j.jcou.2022.101970.

[74] G.G. Stavropoulos, A.A. Zabaniotou, Minimizing activated carbons production cost, Fuel Process. Technol. 90 (7) (2009) 952–957, https://doi.org/10.1016/j.fuproc.2009.04.002.